Thesis for the degree of licentiate of philosophy

A Collinear Angle-Resolved Photoelectron Spectrometer

Instrumental Design and Photodetachment Measurements

Olle Windelius

CHALMERS

Department of Physics
Chalmers University of Technology
Gothenburg, Sweden 2019

A Collinear Angle-Resolved Photoelectron Spectrometer
Instrumental Design and Photodetachment Measurements

Olle Windelius, 2019

Typeset using LaTeX
Department of Physics
Chalmers University of Technology
SE-412 96 Gothenburg, Sweden
Phone: +46 (0)31 772 1000

Printed by Chalmers Digitaltryck
Gothenburg, Sweden 2019

A Collinear Angle-Resolved Photoelectron Spectrometer

Instrumental Design and Photoelectron Measurements

Olle Windelius

Department of Physics
Chalmers University of Technology
SE-412 96 Gothenburg, Sweden

Abstract

For more than half a century, photoelectron spectroscopy has been used to investigate atoms, ions and molecules. Various techniques have been developed in order to measure electron energies and angular distributions using different radiation sources such as lasers and synchrotrons. In this work, a new spectrometer design for measurements of angular distributions of photoelectrons using synchrotron radiation is presented. The design takes advantage of a collinear interaction region, which is two orders of magnitude larger than obtainable with the crossed beams method. The number of events per time unit is thereby substantially increased compared to regular angle-resolved photoelectron spectrometers. This is of great value when the radiation source has a low photon flux and the background is large due to the high photon energy. The spectrometer has been tested on systems where the angular distribution is well-known, in order to develop methods for compensation of the angular transformation between the ion rest frame and the lab frame. Further, a measurement of the angular distribution of a negative ion, P^-, over a wide range of photon energies has been conducted. The results are in agreement with previous measurements and, more importantly, reveal new and valuable information about the theoretical modelling of angular distributions.

The experiments presented show that the spectrometer can be used to measure angular distributions of atomic and molecular ions, and that it can be a valuable

asset at synchrotron beamline endstations. This work also includes a photoionization cross section measurement of Zn^+, performed using the synchrotron at the Advanced Light Source (ALS), Berkeley, CA.

Keywords: Angular distributions, photoelectron spectrometer, photodetachment, photoionization, synchrotron radiation.

List of publications

This licentiate thesis is based on the work presented in Paper I-III. The papers are referred to by capital roman numbers in the text and can be found as Appendices.

I O. Windelius, A. Aguilar, R.C. Bilodeau, A.M. Juárez, I. Rebolledo-Salgado, D.J. Pegg, J. Rohlén, T. Castel, J. Welander and D. Hanstorp.
A collinear angle-resolved photoelectron spectrometer.
Nuclear Instruments and Methods in Physics Research Section B: Beam Interactions with Materials and Atoms, 410:114-152, 2017.

II O. Windelius, J. Welander, A. Aleman, D.J. Pegg, K.V. Jayaprasad, S. Ali, D. Hanstorp.
Photoelectron angular distributions in photodetachment from P^- .
Submitted to Phys. Rev. A, March 2019.

III G. Hinojosa, T.T. Davis, A.M. Covington, J.S. Thompson, A.L.D. Kilcoyne, A. Antillón, E.M. Hernández, D. Calabrese, A. Morales-Mori, A.M. Juárez, O. Windelius and B.M. McLaughlin.
Single photoionization of the Zn II ion in the photon energy range 17.5-90.0 eV: experiment and theory. *Monthly Notices of the Royal Astronomical Society,* 470(4):4048-4060, 2017.

Contents

1

Introduction

Electromagnetic radiation can affect the electric properties of matter, a discovery initially made by Edmond Becquerel in 1839 [1]. Almost fifty years later, Heinrich Hertz investigated electrically charged sparks from metallic surfaces. He discovered that, when irradiated with ultraviolet light, some metals gave off sparks more easily than others [2]. He was, however, not able to explain the phenomenon, and a proper physical explanation had to wait until Max Planck had introduced the concept of quantization of energy in 1900. Around that time, the German physicist Philipp Lenard [3] found that metallic surfaces could emit so called cathode rays, consisting of negatively charged particles now known as electrons, when they were illuminated with light. The energy of these rays could be measured by imposing an electric field in such a way that the ray current drops to zero at the cathode. Classically, the intensity of the incident light should affect the stopping voltage necessary to obtain zero current. What Lenard discovered was that the intensity did not affect the energy of the emitted particles, while decreasing the wavelength resulted in a more energetic beam. This could not be explained by means of classical physics. In 1905, Albert Einstein used Planck's energy quantum concept to explain this photoelectric effect [4] by suggesting that electromagnetic radiation consisted of small units of energy that he called light quanta, later named photons, with an energy proportional to the frequency of the radiation. An electron in a material can absorb one such quantum, and if the absorbed energy is larger than or equal to a certain value, the work function of

the material, the electron can escape the surface. The maximum kinetic energy of the electron then corresponded to the difference between the quantum energy and the work function. These discoveries were the starting point from which the practical applications of light-matter interaction began to develop. Processes where electrons are emitted by incident electromagnetic radiation are studied using photoelectron spectroscopy (PES), a scientific field which has contributed substantially to our present knowledge of the structure and dynamics of atoms, molecules, ions and solids [5, 6]. The first high resolution photoelectron spectra were recorded by Kai Siegbahn in the 1950's [7] using a technique originally called ESCA (Electron Spectroscopy for Chemical Analyses) [8] which more frequently goes by the name XPS (X-ray Photoelectron Spectroscopy), a name which better suits the broader applications [9].

Since then, many different photoelectron spectroscopic methods for various applications have been developed. Some examples are the time-of-flight (TOF) spectrometer [10], magnetic bottle [11], velocity map imaging (VMI) [12, 13] and the photodetachment microscope [14]. There is also a variety of radiation sources available such as lasers, synchrotrons and free electron lasers. In order to enhance performance, the facilities undergo upgrades when new techniques are developed. As an example, chirped pulse amplification (CPA) [15], which rendered a Nobel prize in 2018, is one of the most important improvements of laser technology. This invention boosted the development of pulsed lasers with a high repetition rate, intense radiation and short pulse lengths which have made it possible to study phenomena such as multi-photon excitation of ions where for instance doubly excited states in negative ions are examined [16], or to visualize the electronic motion in atoms [17].

The structure and dynamics of atomic, ionic and molecular systems can be investigated both theoretically and experimentally. This work focuses on negative ions. In such systems, the electron correlation is strong, making analytical treatment very complex. Experimental investigations are therefore necessary in order to test and improve the theoretical models. Since negative ions in general lack bound states, optical spectroscopy can not be utilized. For this reason, PES is the main method to investigate them. The binding energy of the extra electron in a negative ion is called the electron affinity and is of the order of a few eV. The

first electron affinity measurement was made on O^- by Branscomb [18], starting a new branch of experimental physics. Since then, the affinity of the majority of naturally abundant atomic anions have been investigated experimentally. Antimatter, such as the positronium ion Ps^- where an electron-positron system is bound to an additional electron, is also subject to photodetachment experiments [19]. Studies of the ejected electrons can also be performed where the angular distribution is of particular physical interest. Depending on the initial state of the ion, the electron will leave in a superposition of states. This can be seen as an interference, which is dependent on the relative amplitudes and phase shift of the two possible outgoing waves. By measuring the electron yield in directions parallel and perpendicular to the polarization vector of the linearly polarized radiation, the asymmetry parameter, β, which is describing the angular distribution, can be determined. PES can be performed using any radiation source with sufficient photon energy. One of the most commonly used is the synchrotron, which can be utilized to produce high energy photons. This is achieved by using an electron beam which is accelerated in a circular path and thereby emitting radiation. At such facilities, a much wider range of photon energies are available compared to using lasers, making investigations involving inner-shell electrons in atomic systems possible. To this date, most angular distribution measurements performed at synchrotron facilities have used spherical energy analyzers together with a crossed beams geometry where the interaction region is at most a few cubic millimetres. Another technique, VMI, is particularly efficient close to threshold [13, 20] and has recently been used together with synchrotron radiation [21].

Using a crossed beams geometry to measure angular distributions of photoelectrons from an ion beam has its limitations. At a synchrotron radiation source, the low photon flux together with a small interaction volume gives rise to a small signal level. At such facilities, rotation of the polarization vector of the radiation is not always an option, and, even if possible, the purity of the polarization would be affected by the typically low intensity of the photon beam [22]. Hence, a crossed beams geometry in photoelectron angular distribution measurements require setups such as a movable detector, many detectors, or the use of electric fields to collect electrons onto a position sensitive detector. However, these designs do not necessarily increase the data collection rate. Nevertheless, the signal

levels in such an arrangement is low. To this date, only two experimental investigations for measuring photoelectron angular distributions, using a collinear beams geometry, have been performed. First, the setup used by Moussalami *et al.* [23] using sychrotron radiation. In this measurement, a linear source length of the order of 10 mm, inside a cylindrical mirror analyzer (CMA), was used. Second, a collinear angularly resolved spectrometer has been used together with an ion-laser setup [24]. The source length of this device was 250 mm. This measurement was performed by rotating the polarization vector of the light.

To overcome the limitations mentioned above, a new design of an angle-resolved photoelectron spectrometer has been developed [25]. The key features are a high signal to noise ratio, direct asymmetry parameter measurements when the polarization vector is fixed in space, and a large number of detected events per time unit compared with other spectrometers used to this date. The last requirement is met by utilizing a collinear beams geometry, which results in a relatively large interaction volume. The spectrometer was designed for measurements of positive ions using synchrotron radiation.

In this work, the technical details and performance tests of the spectrometer (Paper I), and a photodetachment measurement of a negative ion (Paper II), are presented. In addition, a photoionization experiment of a positive ion using synchrotron radiation is presented (Paper III).

2

Photoelectron spectroscopy

There are several techniques employed in photoelectron spectroscopic measurements [26]. Time-of-flight (TOF) spectrometers [10] separate different photoelectron energies by guiding the electrons to a detector far away from the interaction region. Depending on their initial velocity, electrons will spend different time reaching the detector. By triggering the time recording of an event it is possible to separate different photoelectron energies by their flight time. To achieve a high temporal resolution, this type of detector requires a small interaction region relative to the flight distance. TOF spectrometers can therefore become rather large. An electrostatic analyzer is an ion optical device which can be used to separate electrons with different kinetic energies by bending them using electrical fields [27]. Normally, it is designed to only allow electrons with a certain velocity to pass through and by changing the electrical bias it is then possible to scan the energy distribution and select a specific kinetic energy. In the velocity map imaging method (VMI), electrons ejected in all directions are guided by electrostatic fields onto a position sensitive detector, where all electrons with a certain velocity will end up on the same circle regardless their initial position [28]. In magnetic bottle spectrometers the emitted electrons travel in a strong magnetic field. Since no mechanical work is done on charges by a magnetic field due to the Lorentz force being perpendicular to the momentum of the electrons, it is possible to keep the initial information of the electrons even after a substantial period of time. In such a device, very high collection efficiencies relative to other

photoelectron spectrometers can be obtained [11].
At higher photon energies, the residual atom might end up in an excited state. As a result, the ejected photoelectrons will have different kinetic energies depending on the initial state of the ion and the final state of the atom. In this case it is crucial to be able to separate electrons emanating from different detachment channels in order to characterize the negative ion properly. The most common setup is the crossed beams geometry, where an ion beam is perpendicularly intersected by a photon beam. One advantage of this setup is that the interaction region is well defined in space. As a consequence, the rate at which photodetachment events take place is then relatively low. If, in terms of photon flux, a not so powerful radiation source is used, for instance a synchrotron, the signal level will be low [29]. In order to perform qualitative measurements under such circumstances, the spectrometer design is an important part of the experiment.

2.1 Photodetachment

The interaction between a photon and an atom or ion where electrons are ejected can in a simplified manner be described as follows. Considering an arbitrary atom A, we have for integers n and m,

$$A^{n+} + \gamma \rightarrow A^{(n+m)+} + me^{-}, \qquad m \geq 1, \tag{2.1}$$

where $n \geq 0$ and $n < 0$ correspond to photoionization and photodetachment, respectively.

The photon energies required for photodetachment are at most a few electron volts, while those needed to produce positive ions can be up to several hundred eV depending on the degree of ionization. Therefore, studies of negative ions are easily performed using lasers while atoms and positive ions normally require more powerful radiation sources in terms of photon energy. Atoms and positive ions can, besides being ionized, become excited and emit photons, thereby revealing information about their internal structure. In fact, most of our knowledge about the energy structure of the atomic elements come from this kind of spectral analysis. With a few known exceptions [30, 31], negative ions have no stable excited states below the detachment threshold with a parity that differs from the

ground state. For this reason, spectral analysis is not possible and other methods are therefore necessary in order to investigate them.

2.1.1 Electron affinity

The binding energy of the extra electron in a negative ion is called the electron affinity, in this work denoted by E_A, of the atom. This value is often associated with the ion although it is defined to be the energy gained by the atom when an extra electron is attached. Hence, it is equivalent to the energy needed to detach the extra electron. When a photon of energy $E_\gamma = h\nu$ is used to detach an electron from a negative ion, the ejected photoelectron will carry a kinetic energy given by

$$E_k = h\nu - E_A. \tag{2.2}$$

By measuring the kinetic energy of the electrons ejected at a specific photon energy, the affinity can be determined. With a tunable radiation source it is possible to find the detachment threshold by scanning the wavelength, thereby finding the highest energy at which no photoelectrons are emitted. Another method to increase the resolution is to use the Doppler shift experienced by the ions if the ion-photon beams are collinearly overlapped. In such an experiment, the photon energy leading to photodetachment is measured when the photon and ion beams are counter-propagating. In the ion rest frame, the wavelength of the photons is blueshifted relative to the lab frame. A similar measurement is performed allowing the photon and ion beams travel in the same direction, so that the photon wavelength in the ion rest frame is redshifted, and an average of the two photon energies gives the electron affinity of the atom [32].

2.2 Cross sections

2.2.1 Total cross section

The probability of photodetachment is known as the cross section σ and can be interpreted as the area within which a point-like photon must pass in order to detach the electron. Fig. 2.1 shows a photodetachment cross section, where the

sharp onset is characteristic for negative ions. With increasing photon energy the probability of detachment increases until it reaches a maximum at around $2E_A$. The cross section then falls gradually, making measurements of photodetachment at high photon energies more time consuming. One way to overcome this is to have a large interaction region.

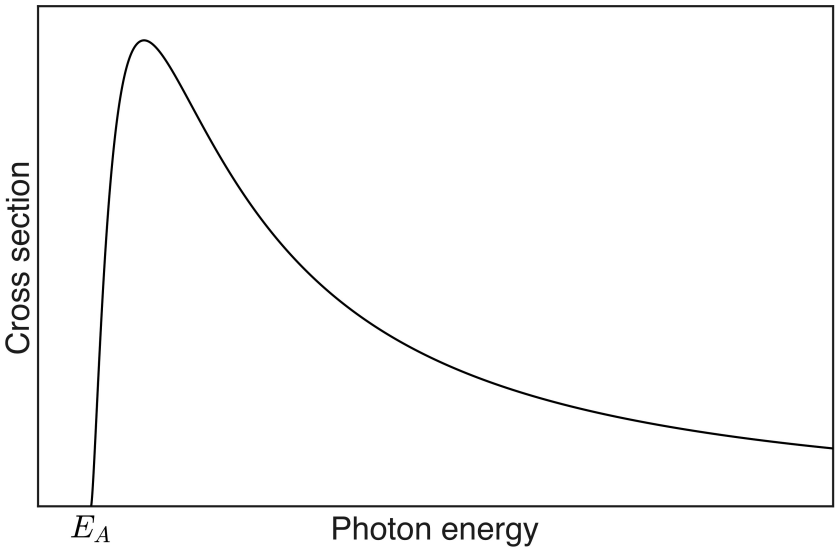

Figure 2.1: Characteristic shape of the total cross section of a negative ion. The maximum occurs at a photon energy of approximately $2E_A$.

Just above the threshold, the behavior of the cross section is described by the Wigner law [33],

$$\sigma \propto E_k^{l+1/2}, \tag{2.3}$$

where E_k is the kinetic energy and l is the angular momentum quantum number of the emitted photoelectron. One consequence of Eq. 2.3 is that at the photodetachment threshold, the cross section of an s-wave will rise quickly while waves carrying a non-zero angular momentum have a less steep onset (Fig. 2.2).

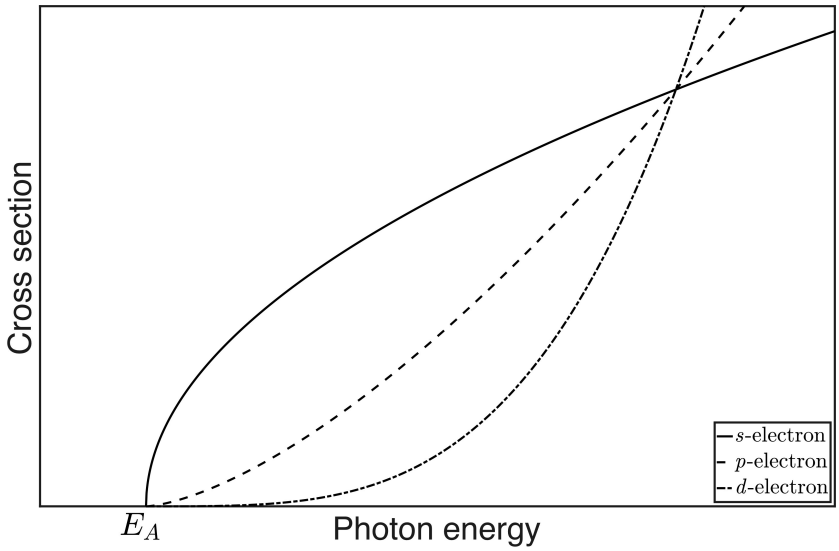

Figure 2.2: Comparison of photodetachment cross section onsets, according to the Wigner law (Eq. 2.3), of partial waves corresponding to different angular momentum.

2.2.2 Partial cross section

The total cross section normally consists of several partial cross sections, each corresponding to the probability for a certain detachment channel. With increasing energy, more channels open up so that a cross section measurement of a specific channel requires an energy analyzer.

2.2.3 Differential cross section

The probability that an electron is ejected in a certain direction in space is called the differential cross section, $\sigma_{diff} = \frac{d\sigma}{d\Omega}$, where Ω is a solid angle. When an electron interacts with linearly polarized electromagnetic radiation, it begins to oscillate along the polarization direction. Classically, the detached electron would leave the ion in a direction parallel to the polarization vector. However, since the electrons are represented by wavefunctions, the probability that they leave the atom in a certain direction depends on the initial state and is described by the quantum mechanical laws governing the transition. It is therefore of significant

interest to investigate the angular distribution of the detached electrons in order to reveal information of the initial state of the ion.

2.3 Angular distributions

The photon has an angular momentum of one, and as a consequence, a photodetached electron will carry an angular momentum given by $\Delta l = \pm 1$. If the initial state corresponds to an s-state, the electron will leave as a p-wave. An initial p-electron, however, will leave as a superposition of an s- and a d-wave. Due to the centrifugal barrier, which scales as $\frac{l^2}{r^2}$, the s-wave dominates close to the threshold [34]. At higher energies, the cross section of the p-wave will become more prominent (Fig. 2.2). Within the dipole approximation, only one parameter is necessary to describe this process. Measurements of the angular distribution of photoelectons is therefore equivalent to investigating this parameter and its energy dependence. The photoelectron intensity $I(\theta)$ in a detector placed at an angle θ with respect to the polarization vector, is proportional to the differential cross section of photodetachment from an unpolarized target. This dependence is given by [35]

$$I(\theta) \propto \frac{d\sigma}{d\Omega} = \frac{\sigma}{4\pi}(1 + \beta P_2(\cos\theta)), \tag{2.4}$$

where P_2 is the 2^{nd} degree Legendre polynomial, $P_2(x) = \frac{1}{2}(3x^2-1)$. The asymmetry parameter β is a function of the phase shift, $\delta_{l+1} - \delta_{l-1}$, of the two interfering outgoing waves, and the radial dipole matrix elements $R_{l\pm1}$. This dependence, originally derived by Bethe [36] and later generalized by Cooper and Zare from whom it has achieved its name, the Cooper-Zare formula, is given by

$$\beta = \frac{l(l-1)R_{l-1}^2 + (l+1)(l+2)R_{l+1}^2 - 6l(l+1)R_{l-1}R_{l+1}\cos(\delta_{l+1} - \delta_{l-1})}{(2l+1)[lR_{l-1}^2 + (l+1)R_{l+1}^2]}. \tag{2.5}$$

The matrix elements $R_{l\pm1}$ are not straightforwardly calculated, but Hanstorp *et al.* [37] derived an approximate form of Eq. 2.5,

$$\beta = \frac{2A_2\varepsilon(A_2\varepsilon - 2c)}{1 + 2A_2^2\varepsilon^2}, \tag{2.6}$$

where A_2 is the relative size of the matrix elements R_0 and R_2, $c = \cos(\delta_{l+1} - \delta_{l-1})$ is a measure of the phase shift, and ε is the photoelectron energy. The parameter

A_2 is related to the size of the ion. When performing measurements of angular distributions over a range of photoelectron energies, it is thus possible to fit experimental data to Eq. 2.6 using only A_2 and c as fitting parameters. The asymmetry parameter is in the range $-1 \leqslant \beta \leqslant 2$. Here, $\beta = -1$ corresponds to the electron leaving as a pure $\sin^2\theta$-wave, $\beta = 0$ is an isotropic distribution and $\beta = 2$ corresponds to a pure $\cos^2\theta$-wave. It is straightforward to show that the intensity, depending on the sign of β, can be written on the normalized forms

$$I(\theta) = (1 - Q_1)\sin^2\theta + Q_1, \qquad -1 \leq \beta < 0, \tag{2.7}$$

$$I(\theta) = (1 - Q_2)\cos^2\theta + Q_2, \qquad 0 < \beta \leq 2, \tag{2.8}$$

where Q_1 and Q_2 are positive constants for a given non-zero value of β. Thus, $I(\theta)$ can be regarded as consisting of one isotropic part, independent of the emission angle θ, and one anisotropic part. If $\beta = 0$, $I(\theta)$ is constant so that $Q_1 = Q_2 = 1$.

It should be mentioned that $P_2(\cos\theta)$ vanishes when $\cos\theta = \frac{1}{\sqrt{3}}$. The photoelectron intensity given by Eq. 2.4 is therefore independent of β at this so called magic angle $\theta_0 = \cos^{-1}(\frac{1}{\sqrt{3}}) \approx 54.7°$ (Fig. 2.3). This angle can be used in angle-resolved measurements to identify systematic errors not related to the photodetachment process. Another example is nuclear magnetic resonance spectroscopy (NMR) where some of the nuclear magnetic interactions have an angular dependence of the 2^{nd} order Legendre polynomial [38].

Fig. 2.4 shows the energy dependence of the asymmetry parameter for a p-electron detachment from a negative ion, where the residual atom is left in the ground state. If the two outgoing s- and d-waves have a phase shift of exactly π, they experience destructive interference in a direction parallel to the polarization vector of the incident radiation. This corresponds to $\beta = -1$ if their amplitudes are equal. The shape is characteristic for p-valence negative ions. At energies above the minimum, the d-wave will be dominant and β will approach 1 with increasing energy until new channels open.

2.3.1 An experimental method

Several techniques and apparatuses can be employed in measuring the angular distribution of photoelectrons. In this section, theoretical aspects of the experimental method used in this work are discussed. It is important to point out that

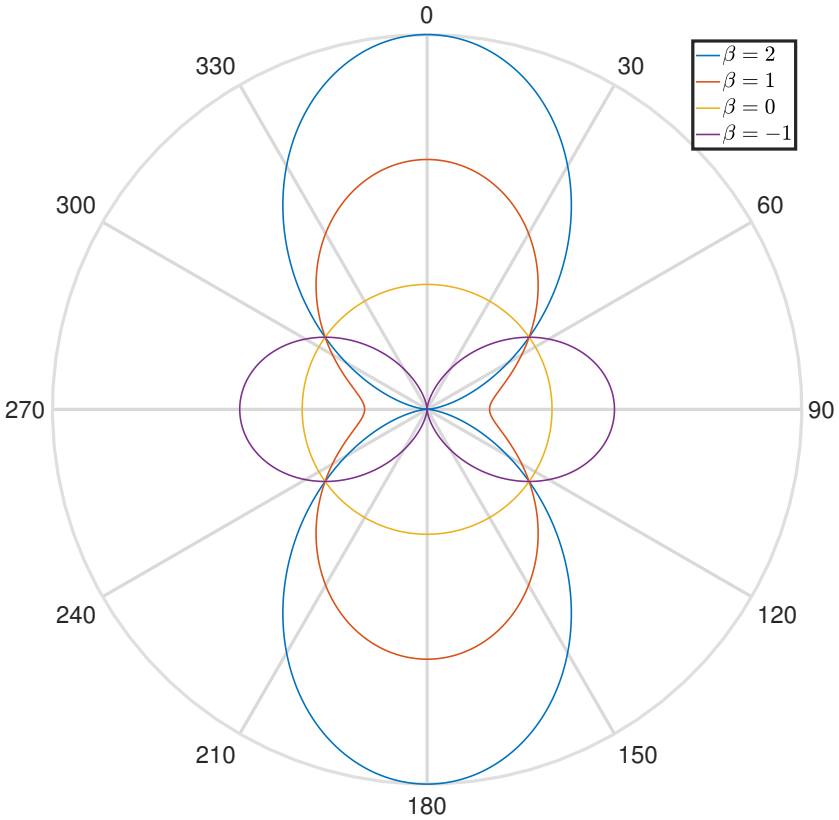

Figure 2.3: Polar plot of Eq. 2.4 for four different values of β. All curves intersect at the magic angle $\theta_0 \approx 54.7°$.

it is here assumed that the photoelectron source and the detector are at rest with respect to each other. Transformation from the lab frame, where the detector is placed, to the rest frame of the physical system under investigation, will be described in Section 2.4.1.

The photoelectron yield at a fixed photon energy can be measured while rotating the polarization vector by discrete steps. The data points $I(\theta)$ can then be fit to the right hand side of Eq. 2.4. By doing so, the asymmetry parameter can be obtained directly. In the ideal case, however, it is only necessary to simultaneously measure the intensity parallel and perpendicular to the polarization vector. To see this, consider the normalized forms of $I(\theta)$ given by Eq. 2.7 and 2.8. As Fig. 2.5 shows, the anisotropic part can be treated as purely $\sin^2\theta$- or $\cos^2\theta$-distributed, respectively. The isotropic parts, Q_1 and Q_2, are given by

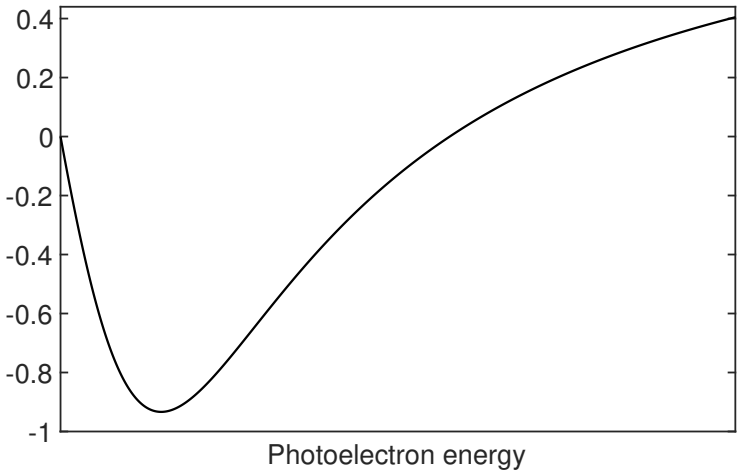

Figure 2.4: The general shape of the energy dependence of β for a p-electron detachment. Due to selection rules, the electron will leave the negative ion as an s- or a d-wave. At the photodetachment threshold, the electron leaves as a pure s-wave with $\beta = 0$, while the interference with the d-wave varies with increasing photon energy. The depth of the minimum is dependent on the phase shift between the two waves, while the position along the energy axis depends on the parameter A_2 (Eq. 2.6).

the normalized photoelectron yield at $\theta = 0°$ or $\theta = 90°$, respectively. At these angles, the intensities given by Eq. 2.4 become

$$I(0°) = k(1 + \beta), \tag{2.9}$$

and

$$I(90°) = k(1 - \frac{\beta}{2}), \tag{2.10}$$

respectively. The proportionality constant k is the same in both cases for a given photoelectron energy, but is dependent on the differential cross section. Using Eq. 2.9 and Eq. 2.10, we see that

$$Q_1 = \frac{I(0°)}{I(90°)} = \frac{1+\beta}{1-\frac{1}{2}\beta}, \qquad \beta < 0, \tag{2.11}$$

$$Q_2 = \frac{I(90°)}{I(0°)} = \frac{1-\frac{1}{2}\beta}{1+\beta}, \qquad \beta > 0. \tag{2.12}$$

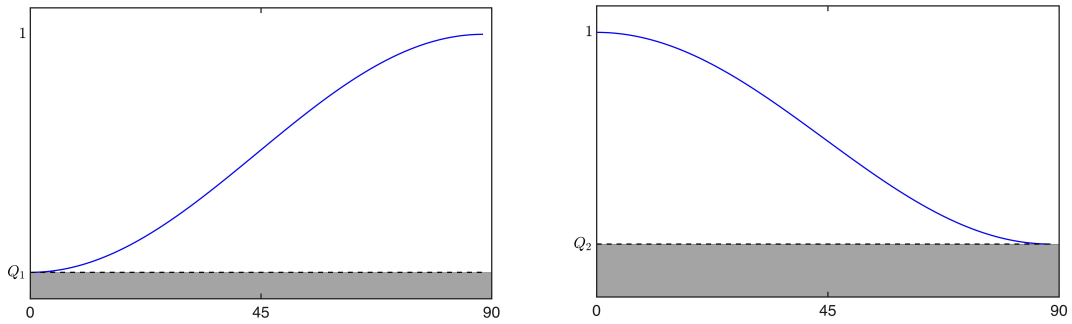

(a) $I(\theta)$ when $\beta < 0$.

(b) $I(\theta)$ when $\beta > 0$.

Figure 2.5: General shape of the photoelectron intensity as function of emission angle, according to the two cases described by Eq. 2.7 and 2.8. The yields are normalized with respect to the maximum intensity. The shaded areas are the isotropic parts of the intensities.

Solving Eq. 2.11 and 2.12 for β, the asymmetry parameter in each of the two cases can thus be calculated directly,

$$\beta = \frac{Q_1 - 1}{1 + \frac{1}{2}Q_1}, \qquad I(0^\circ) < I(90^\circ), \tag{2.13}$$

$$\beta = \frac{1 - Q_2}{Q_2 + \frac{1}{2}}, \qquad I(90^\circ) < I(0^\circ). \tag{2.14}$$

This leads to the conclusion that the experimental task of finding the asymmetry parameter can be reduced to finding the values Q_1 and Q_2.

2.4 The kinematic effect

In Section 2.3.1, a method to obtain the asymmetry parameter was described. However, it was assumed that the detector and the photoelectron source were at rest with respect to each other. In general, this is not the case. In the rest of this work, the source of the photoelectrons is an ion beam moving with a non-zero velocity. The ions are moving relative to the detector when they emit an electron. Due to this motion, the electron emission angles and velocities in the Ion rest Frame (IF) are changed when viewed in the Lab Frame (LF), in which the measurements are made. This change is called the kinematic effect [39], and has to

be taken into account when the asymmetry parameter of a system is investigated. In this work, the angle ψ denotes the LF angle between the polarization vector and the direction of detection.

A photoelectron which is detected in a direction making an angle of 90° relative to the ion velocity vector in the LF, has to have been ejected with an IF velocity making a larger angle, $90° + \alpha$, relative to the ion velocity (Fig. 2.6).

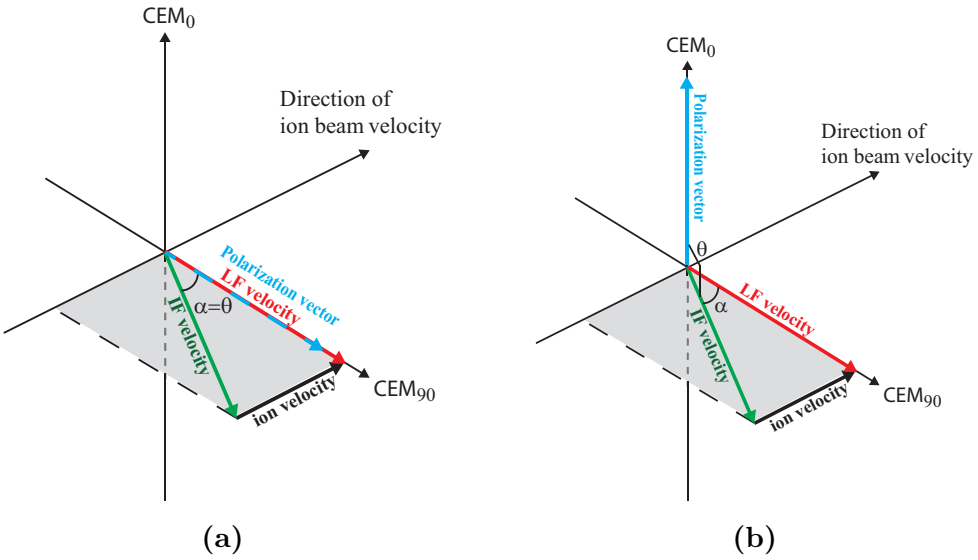

Figure 2.6: (a) If the polarization vector of the photon beam points towards CEM_{90} in which a photodetached electron is detected, the LF detection angle $\psi = 0°$ and the IF emission angle $\theta = \alpha$ are different due to the kinematic effect. (b) In the case where the LF angle $\psi = 90°$, electrons detected in CEM_{90} have been emitted at an angle $\theta = 90°$ with respect to the polarization vector of the photon beam, regardless of the kinematic angle α.

If the polarization vector of the photon beam points towards the detector, the emission angle with respect to the polarization direction will be measured as $\psi = 0°$ in the LF, while it is $\theta = \alpha$ in the IF (Fig. 2.6a). If the polarization vector is perpendicular to the detection direction in the LF, $\psi = \theta = 90°$ (Fig. 2.6b). In addition, the discrepancy between the LF and the IF angles will be a function of detection and polarization angles.

A way to visualize the kinematic effect is to see how the angular distribution of the detached electron changes through the transformation from the IF to the LF. As shown in Fig. 2.7, the torus-shaped $\sin^2\theta$-distribution becomes distorted in the LF.

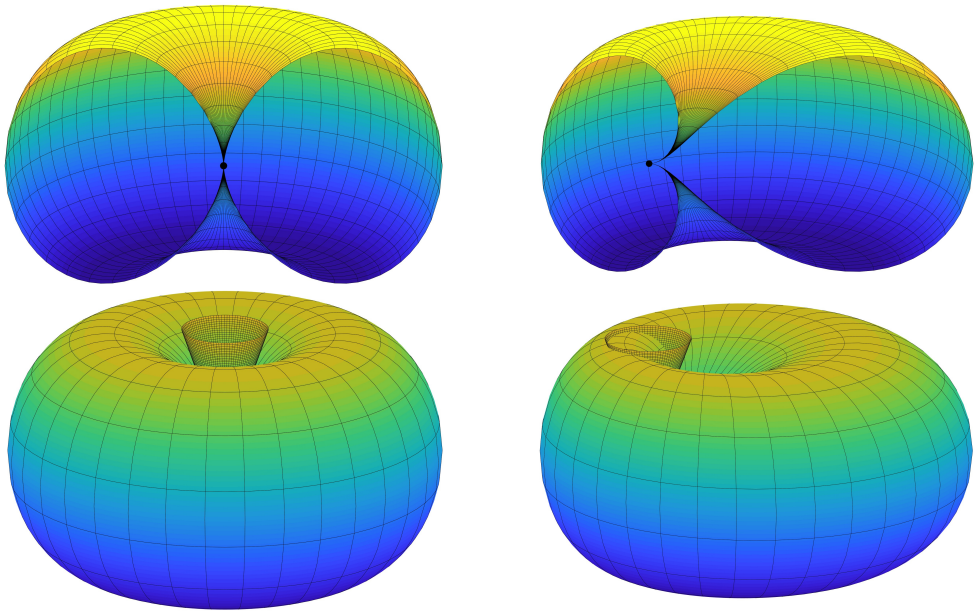

(a) A $\sin^2\theta$-distribution as viewed in a comoving frame.

(b) An IF $\sin^2\theta$-distribution as viewed in the LF.

Figure 2.7: Due to the kinematic effect, a $\sin^2\theta$-distribution in the IF (left) will be distorted when viewed in the LF (right). The cones illustrate a solid angle within which electrons would be detected by a CEM facing downward, placed parallel to the polarization of the incident radiation ($\psi = 0°$, upward in the picture). If the CEM and the ions were at rest with respect to each other, the CEM would have close to zero yield (lower left). The kinematic effect causes an asymmetry in the lab frame, which in turn allows the CEM to detect electrons with $\theta > 0°$ at $\psi = 0°$ (lower right). The black dots indicate the ions from which the electrons are detached. The ion velocity vector points to the right.

If the velocity of the emitted photoelectron is large compared with the ion velocity, that is, for photon energies far above the photodetachment threshold, the

kinematic effect is small. To obtain the correct value of β, that is, the value of the asymmetry parameter in the IF, it is necessary to perform a transformation from the LF to the IF.

2.4.1 Kinematic correction

A transformation between the two frames of reference has been developed with the aid of the computer simulation software SIMION [40]. This correction procedure takes into account both the kinematic effect, and the geometric properties of the spectrometer used in the experiment. In this section, the procedure is described in general terms. It is applicable to any angular distribution measurement where the detection process can be simulated. Consider first the case where $I(0°) < I(90°)$. Normalizing to the intensity at the LF angle $\psi = 90°$, where the kinematic effect is negligible, the relative minimum intensity m at $\psi = 0°$ is obtained (Fig. 2.8). By performing a computer simulation of the expected detection process, with a pure $\sin^2\theta$-distribution of IF emission angles as input, a simulated LF yield $\widetilde{Q}_1$ is determined (inset of Fig. 2.8). This value can then be used to correct the experimentally obtained LF value m for the kinematic effect, also taking geometric properties of the detection system used in the experiment into account, and calculate the IF value Q_1.

$$m = Q_1 + \widetilde{Q}_1(1 - Q_1), \tag{2.15}$$

$$Q_1 = \frac{m - \widetilde{Q}_1}{1 - \widetilde{Q}_1}. \tag{2.16}$$

The β in the IF, that is, the asymmetry parameter of the physical system under investigation, can now be calculated using Eq. 2.13.

Consider now the other case, where $I(0°) > I(90°)$. Here, it is not possible to normalize with respect to the maximum yield, since this occurs where the kinematic effect is at its largest (Fig. 2.9). Hence, the relative minimum yield in the LF, m, will not depend on the kinematic effect directly. The transformation described above will therefore not lead to a correct value of β. Fortunately, this situation occurs when the photoelectron energy is relatively large. With increasing energy, the kinematic effect will get smaller. The necessary correction

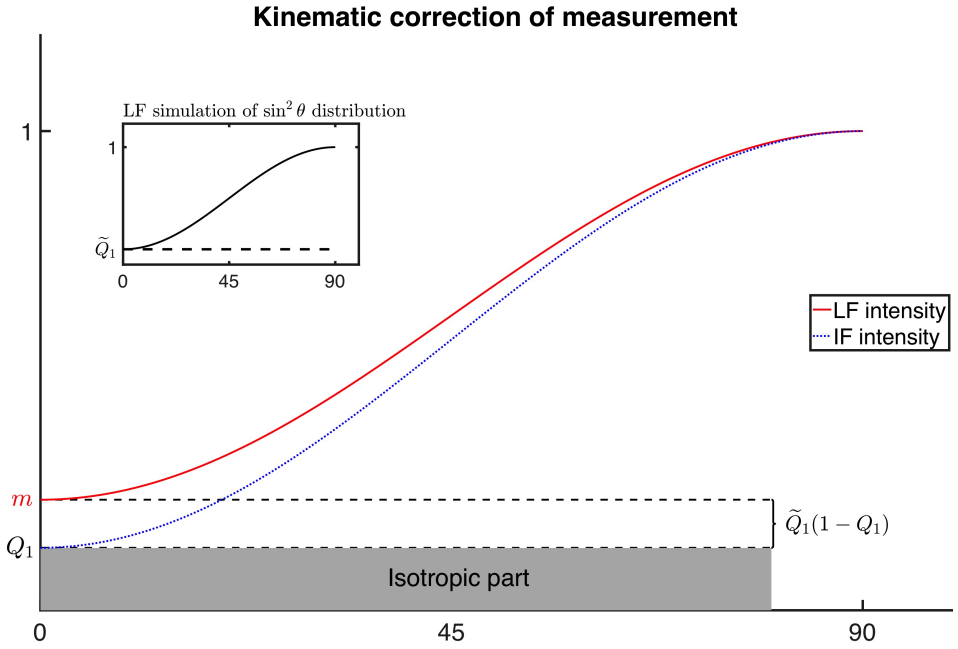

Figure 2.8: By performing a photoelectron angular distribution measurement at a given photon energy, the value m is obtained. A simulation of the detector used in the experiment, with a pure $\sin^2\theta$-distribution in the IF as input, gives the LF term $\widetilde{Q}_1$ (inset). The IF value Q_1 from the experimental investigation is then calculated using Eq. 2.16. By inserting this value into Eq. 2.13, the asymmetry parameter of the system can be obtained.

due to the discrepancy in the detection and emission angles between the LF and IF will therefore also be small. One way to obtain an estimate of the correction in this case is to use the simulation of the experiment in a different manner. The measurement gives rise to an experimental LF value of $\widetilde{\beta}_{exp} = \frac{1-m}{m+\frac{1}{2}}$, according to Eq. 2.14. As input in the simulation, a range of IF angular distributions corresponding to $\beta_i, i = 1...n$, where $\beta_1 < \widetilde{\beta}_{exp} < \beta_n$, can be used. The simulation outputs will then be a range of values $\widetilde{Q}_{2_i}$, which are inserted into Eq. 2.14, and the thus obtained $\widetilde{\beta}_{i_{sim}}$ are compared with $\widetilde{\beta}_{exp}$. For some $p \in [1, n]$, $|\widetilde{\beta}_{p_{sim}} - \widetilde{\beta}_{exp}|$ takes on a minimum value. The β_p used in the simulation to produce $\widetilde{\beta}_{p_{sim}}$ then corresponds to the corrected asymmetry parameter in the IF.

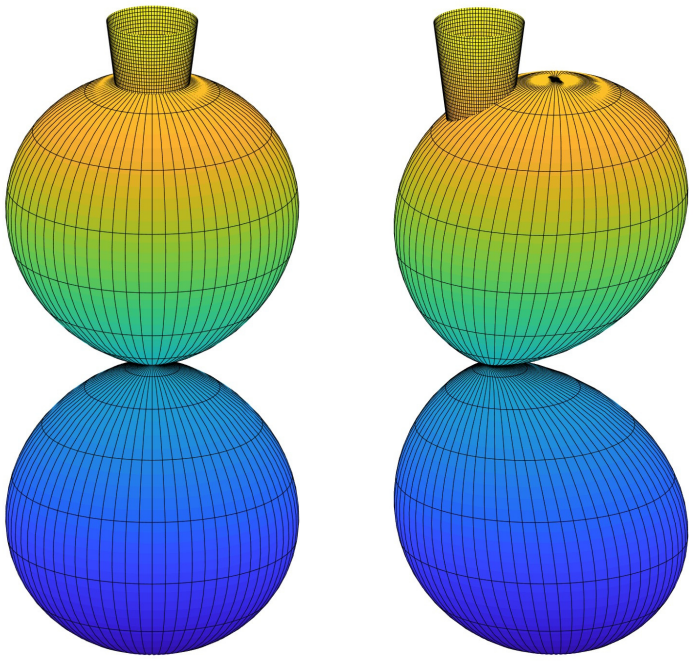

(a) A $\cos^2\theta$-distribution as viewed in a comoving frame.

(b) When viewed in the LF, the distribution is distorted.

Figure 2.9: For a $\cos^2\theta$-distribution, in the transformation from the IF to the LF, the photoelectron intensity in detectors in the vertical plane will be reduced due to the kinematic effect. The yield in detectors in the horizontal plane will not be affected. The cones illustrate a solid angle within which electrons would be detected by a CEM facing downward, placed parallel to the polarization of the light ($\psi = 0°$, upward in the picture). The ion velocity vector points to the right.

3

A PhotoElectron Angle-Resolved Linear Spectrometer

3.1 Basic design concept

As mentioned in the introduction, one of the challenges in performing angular distribution measurements at synchrotron facilities is the low signal to noise ratio in the case of a crossed beams geometry. The simplest way to increase the data collection rate is to create a collinear interaction region where the ion beam and the photon beam are merged along a distance of several centimeters. One drawback with a collinear setup is that the photoelectrons are emitted along a long distance rather than from a single point. A consequence of the extended source of electrons is lack of energy and angular resolution. From this it is clear that a collinear spectrometer will in general not be suitable for high resolution measurements, but will be advantageous, for example, when investigating the behaviour of the asymmetry parameter in a wide energy interval. On the other hand, a collinear interaction region allows for measurements of many emission angles simultaneously since events are detected in a plane perpendicular to the ion-photon beams. As mentioned in Section 2.3.1, it is only necessary to measure the photoelectron yield at 0° and 90° with respect to the polarization direction

in order to determine the asymmetry parameter β. Therefore, an angle-resolved spectrometer stationed at a radiation source with fixed polarization could, in principle, be constructed using two fixed mutually perpendicular detectors. It would then be necessary to know the detection efficiency in both detectors. On the other hand, one can partly compensate for any differences in the efficiencies of the detectors by using four instead of two, placing them pairwise parallel and opposite each other and using a normalization technique that will be described in Section 4.1.1. It is also very useful to remove lower energy electrons that arise from the photodetachment channels involving excited states of the parent atom. This can be achieved by incorporating a high pass energy filter.

3.2 Mechanical design

With the above considerations in mind, PEARLS (PhotoElectron Angle-Resolved Linear Spectrometer) was designed and manufactured at the Advanced Light Source ALS in Berkeley, California, and later shipped to the Göteborg University Negative Ion Laser LAboratory GUNILLA for performance tests. Here, a short overview of the spectrometer is presented, while a more detailed description can be found in Paper I [25]. The design of PEARLS originated from a single graphite tube spectrometer [41]. One key improvement relative to the original design is the ability to measure the asymmetry parameter β directly, without having to rotate the polarization vector of the radiation. This is achieved by incorporating a detector plane with four CEMs that define the directions up, down, left and right (Fig. 3.1). The computer software SIMION was used in the design process to optimize the collection efficiency and the overall performance of the spectrometer.

The basic concept of PEARLS is that the ion beam and the photon beam overlap within the graphite tube in the center of the spectrometer which is considered field free. The electrons detached in the photon-ion interaction escape through small holes along the side of the tube and enter a detector box with CEMs at the far side (Fig. 3.2).

There are also some electrodes outside the graphite tube that can be used to guide the electrons toward a CEM. A high pass energy filter is also included in the design in order to reject lower energy electrons. The linearly extended design of

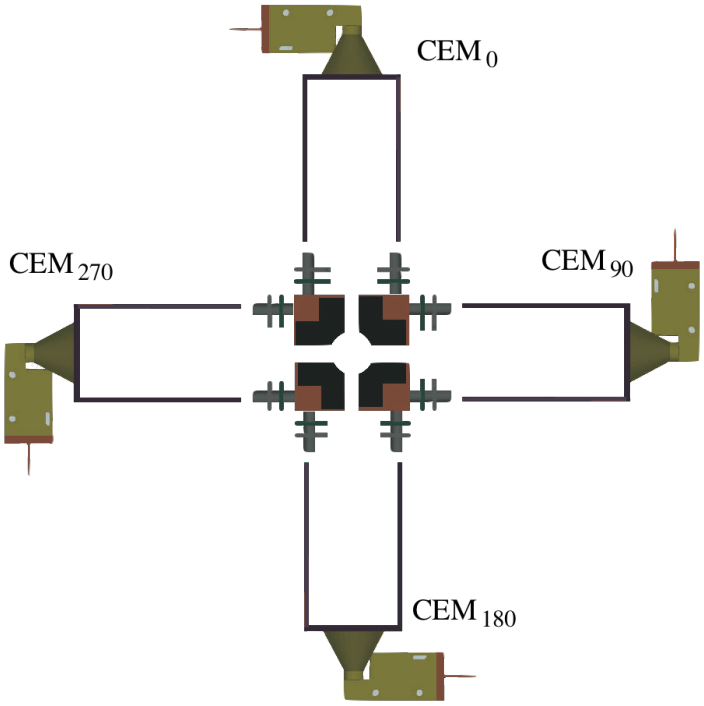

Figure 3.1: Schematic cut-through view of PEARLS, where one of the four identical detector planes is shown. The angular labels on the CEMs are relative to the upright vertical lab frame direction as seen along the ion-photon beam direction.

PEARLS provides an interaction region two orders of magnitude larger than with a crossed beams setup. Relative to VMI, which uses electric fields and a TOF detector to collect all photoelectrons in all directions, PEARLS allows the electrons to be emitted in a field free region within the graphite tube before escaping through the holes. Following this, an electric field guides them towards a CEM. Although PEARLS only collects electrons at certain emission angles, the total number of detected photoelectrons per unit time is considerably larger than in a crossed beams geometry. As discussed in Section 2.3.1, all significant information of the asymmetry parameter β is contained in the photoelectron yield at 0° and 90° with respect to the polarization vector of the radiation. Therefore, collecting all emitted electrons will not provide a substantial increase in the accuracy of the measured value of β. Materials were carefully chosen to allow the detector to function in an ultra high vacuum environment, minimize patch fields and contact

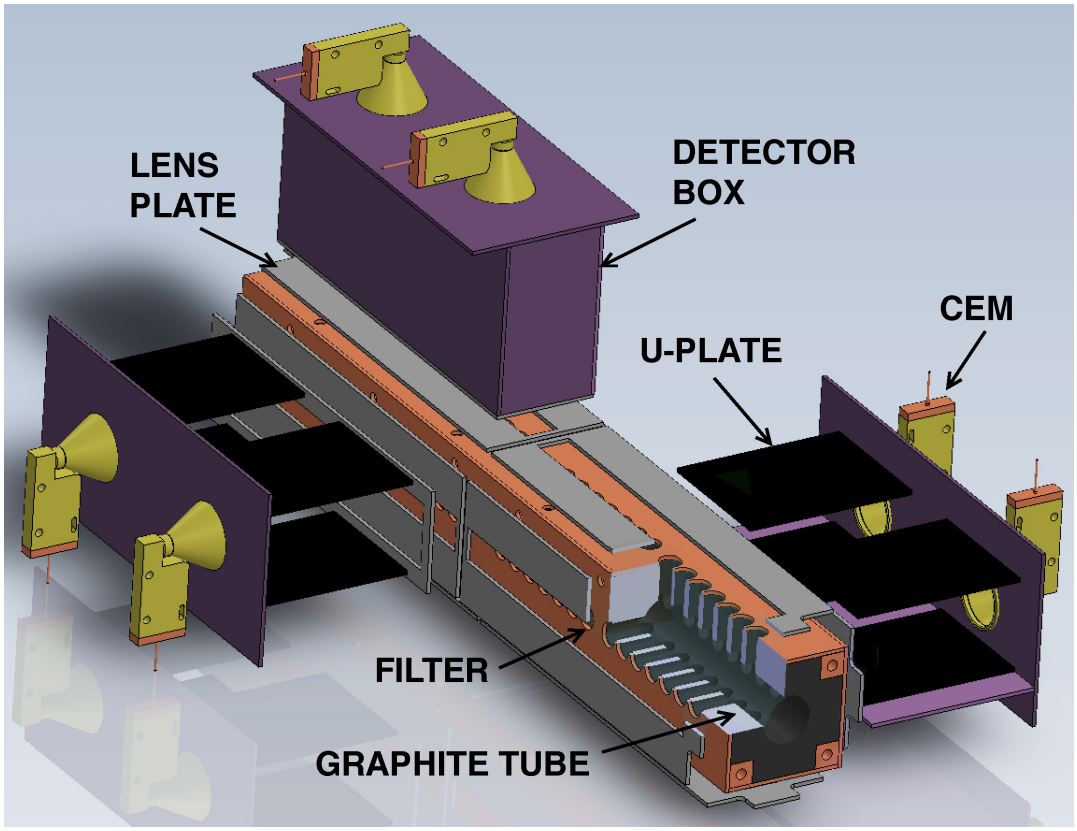

Figure 3.2: Cutaway view of PEARLS where the interior of the spectrometer is shown. The filter consists of a fine copper mesh placed at the exit holes. The lens plate and the U-plate, the name of the latter referring to its geometrical shape, can be electrically biased and used to guide the electrons toward the CEMs.

potentials. The full assembly of PEARLS is shown schematically in Fig. 3.3.

3.3 Simulations

Computer simulations using the ion optics software SIMION were performed in order to investigate the limitations, behaviour and characteristics of PEARLS. These were made prior to manufacturing, but also alongside experiments, as a means to investigate the performance, and to correct for the kinematic effect and the geometry of the detector when evaluating experimental data.

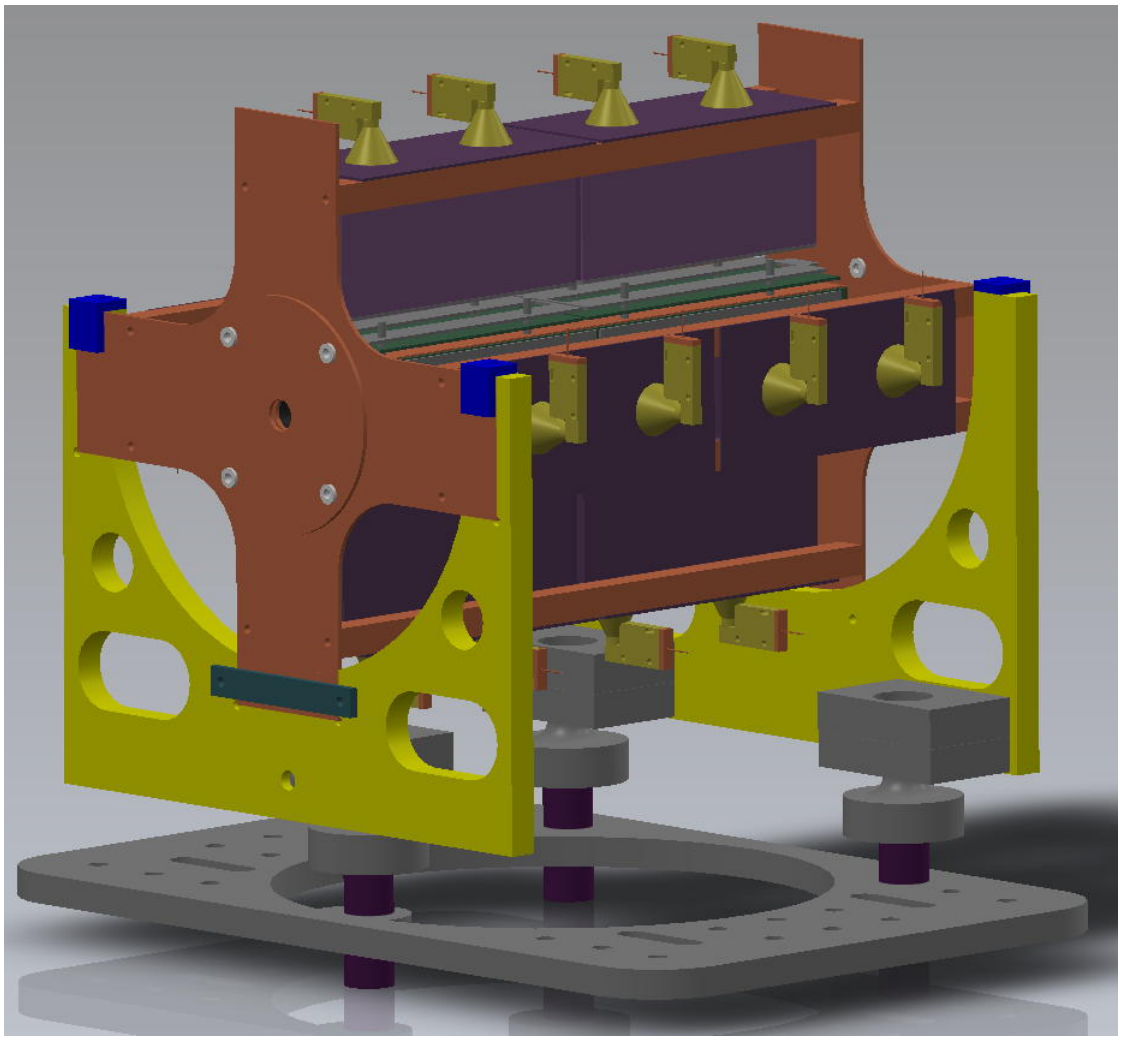

Figure 3.3: A schematic of the complete assembly of PEARLS showing 8 CEMs in the horizontal plane and another 8 in the vertical plane. Thus a set of 4 CEMs define a detector plane, perpendicular to the ion-photon beam direction. The CEMs at the entrance to the apparatus are labelled 1-4 in a clockwise manner, starting at the top, corresponding to CEM_0-CEM_{270} in the detector plane shown in Fig. 3.1. The CEMs in the next detector plane are labelled 5-8, and so forth.

3.3.1 High pass filter

As shown in Fig. 3.2, PEARLS is equipped with electrodes that can be individually electrically biased to function as lenses and filters. One of the key features in

the present setup is the high pass filter which consists of a copper mesh covering the exit holes in the graphite tube. Fig. 3.4 shows a simulation of the trajectories of photoelectrons of two different energies with an unbiased and a biased filter, respectively. The low energy electrons are completely repelled by the mesh which is placed where the electrons exit the graphite tube.

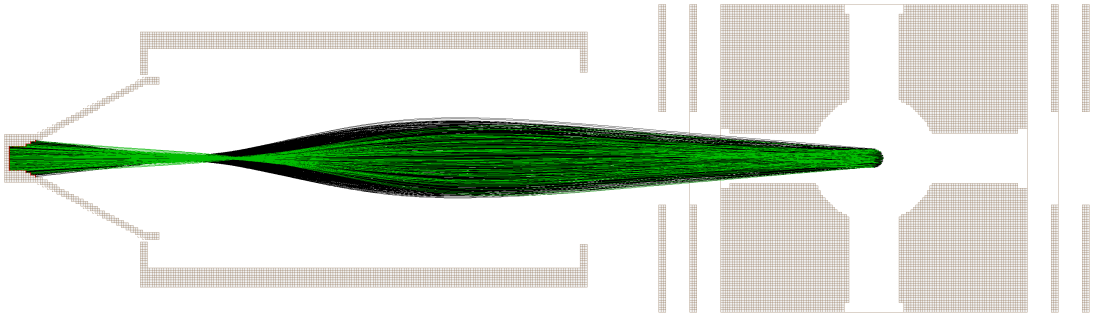

(a) Unbiased mesh, electrons with a kinetic energy of 0.95 eV (green) and 2.35 eV (black) are transmitted from the graphite tube and reach the CEM on the left.

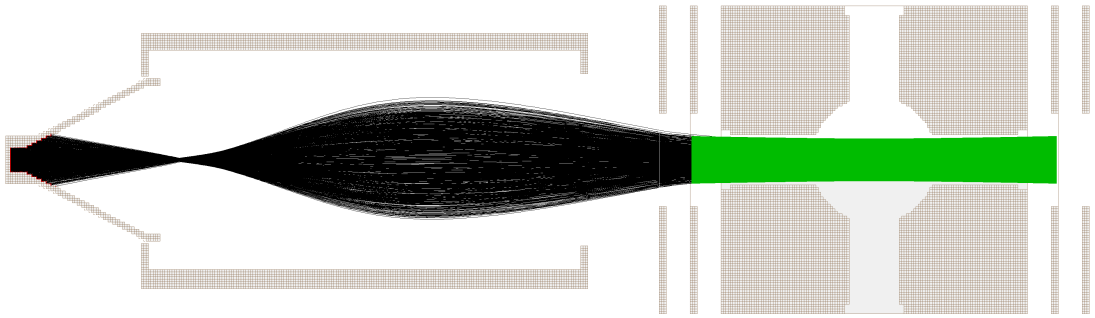

(b) Mesh biased at -1 V, where the mesh potential is sufficiently high to keep the low energy electrons from exiting the graphite tube.

Figure 3.4: Simulations of the trajectories of electrons passing through, or being repelled by, the high pass energy filter.

In Paper I the functionality of the high pass filter was demonstrated experimentally. In Fig. 3.5, the experimental data is compared to a simulation. The blocking of the low energy electrons is represented by a very distinct step in the signal in both data sets.

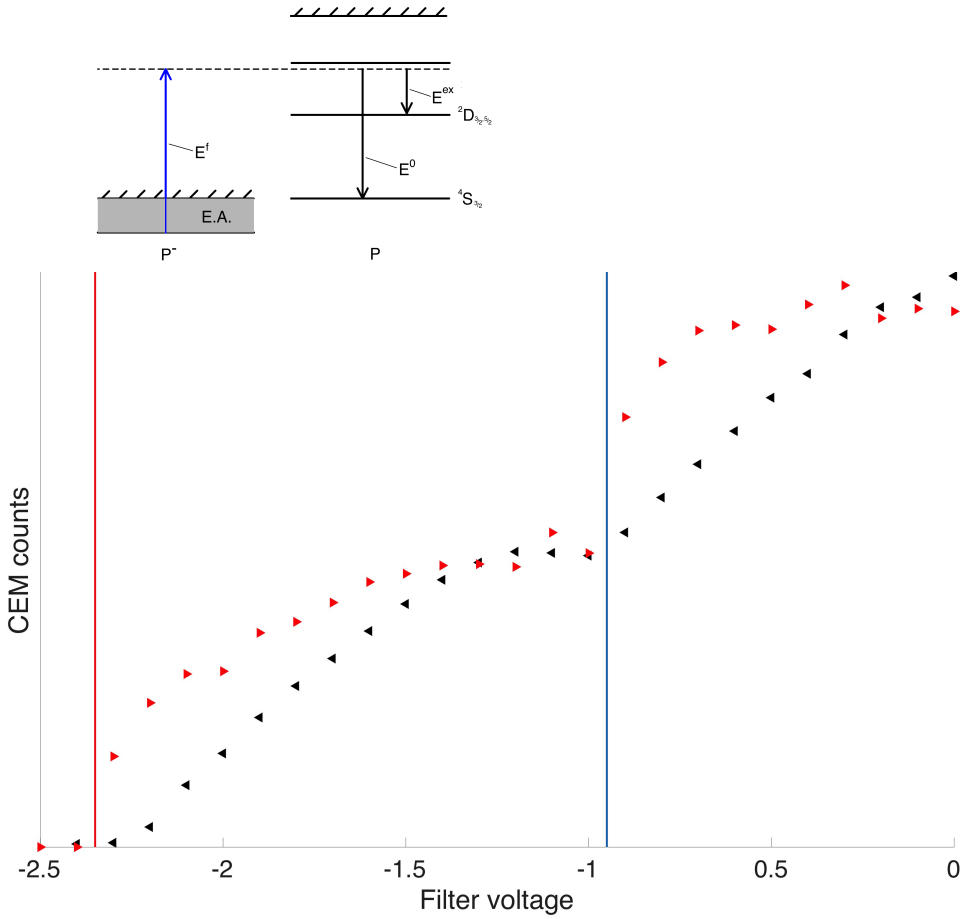

Figure 3.5: The upper diagram shows a schematic of the ground state and first excited states of P. If the photon energy E^f is large enough it will be able to leave the residual atom in both states. The plot shows the normalized yield of photoelectrons from P^- when electrons of two different energies are present. The red triangles represent simulated data while the black triangles correspond to experimental data. The blue vertical line indicates the energy of the electrons corresponding to the excited state at $E^{ex} \approx 0.95$ eV and the red vertical line is the ground state photoelectron energy $E^0 \approx 2.35$ eV.

3.3.2 Kinematic effect and correction

The kinematic effect, described in Section 2.4, increases significantly as the photoelectron energy approaches zero. Fig. 3.6 shows histograms of the angular distribution in the IF of electrons reaching CEMs at $\psi = 0°$ and $\psi = 90°$ (LF angles) relative to the polarization vector of the radiation.

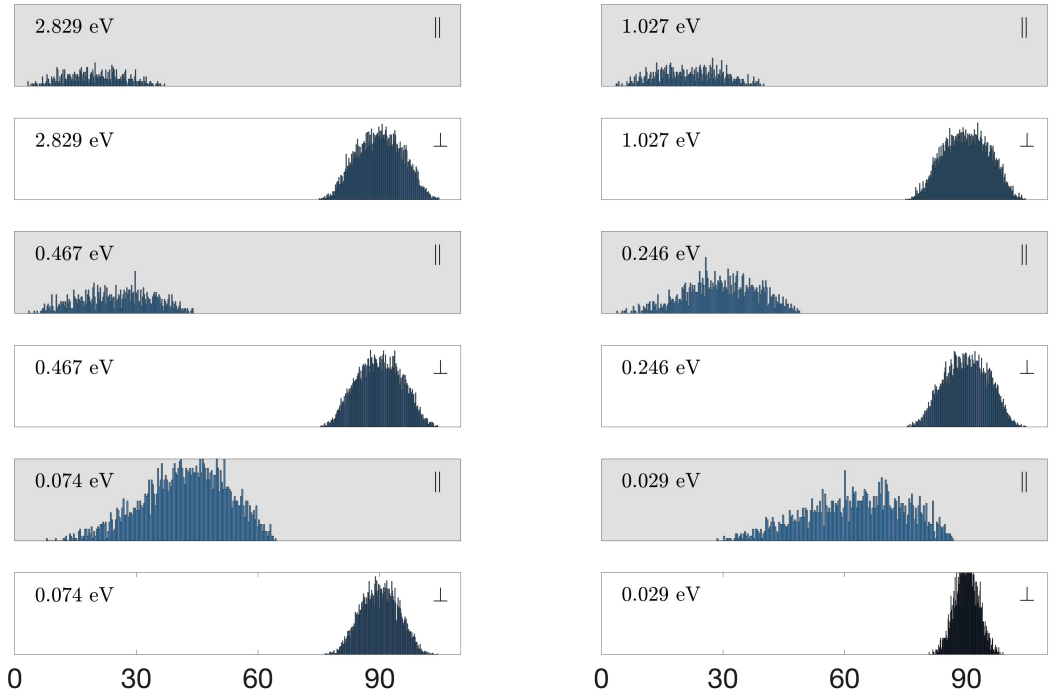

Figure 3.6: A simulation showing the kinematic effect at six different photoelectron energies. Pairs of histograms representing the number of $\sin^2\theta$-distributed photoelectrons detected as a function of angle of emission in the IF are shown. The upper (lower) graph in each pair corresponds to the CEMs placed parallel (perpendicular) to the polarization vector in the LF. As seen in the bottom right, photoelectrons with $E_k = 0.029$ eV detected at $\psi = 0°$ in the LF are emitted in the range $28° \leq \theta \leq 87°$ in the IF, thus showing a very large kinematic effect.

At 29 meV, some of the electrons detected at $\psi = 0°$ in the LF are emitted at an angle $\theta > 80°$ in the IF. The theoretical limit for detection for the settings used in this simulation occurs at 0.0302 eV, but photoelectrons are still being detected

in both directions at a slightly lower energy. This is due to the size of the holes in the graphite tube, which allow electrons with an IF velocity smaller than the ion beam velocity to reach a CEM, even though in such a case the LF velocity vector does not point straight into the CEM. The kinematic correction $\widetilde{Q}$ (inset of Fig. 2.8) will increase rapidly at low energies (Fig. 3.7).

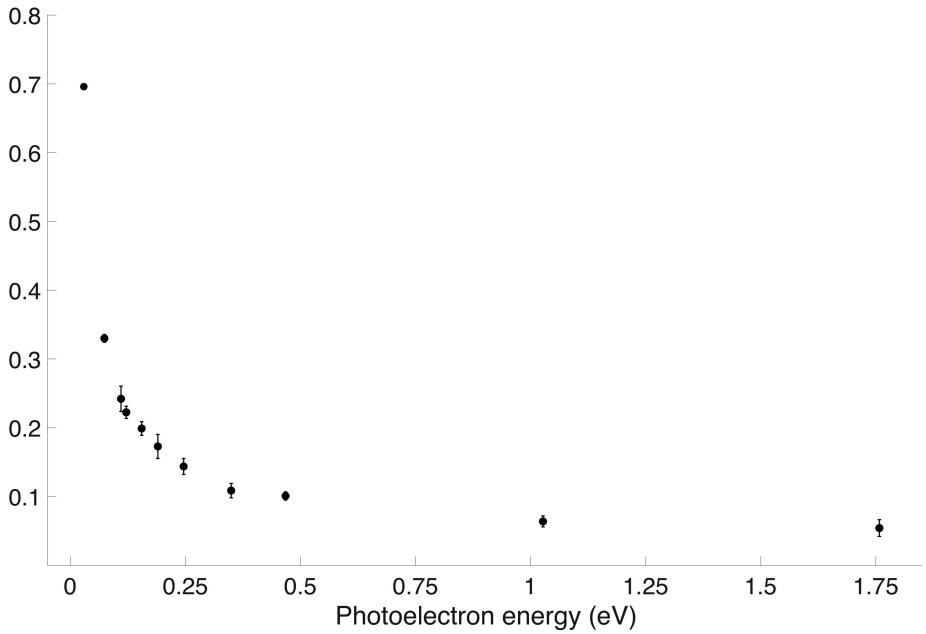

Figure 3.7: Simulation of the correction term $\widetilde{Q}$, described in Section 2.4.1, as a function of electron energy. A pure $\sin^2\theta$-distribution of photoelectrons was used in the simulation which covers a range of photon energies. As the graph shows, the kinematic and acceptance angle correction $\widetilde{Q}$ increases significantly at lower electron energies, and the geometrical properties of the spectrometer does not allow very low energy electrons to escape the graphite tube. Below 29 meV, no electrons were detected in the simulations.

Therefore, the reliability of a PEARLS measurement close to the photodetachment threshold decreases, as the necessary correction for the kinematic effect increases, and as the slow electrons tend not to be able to exit the graphite tube. Thus, it can be concluded that, close to the photodetachment threshold, the necessary correction due to the kinematic effect is too large for PEARLS to be of

practical use. On the other hand, it can be argued that since the value of β tends to zero almost linearly for decreasing values of the photoelectron energy below the minimum (Fig. 2.4), measurements in this energy range are not carrying any valuable information.

4

Tests of detector performance

The PEARLS spectrometer was initially assembled at ALS and mounted in a stand-alone vacuum chamber. A vacuum reaching 10^{-9} Torr was achieved by a turbo pump and an ion pump. The electrical connections were checked for crosstalk, signal shape and strength using a Phillips Model 417 NIM pocket pulser. PEARLS was then disassembled and shipped to the University of Gothenburg, where both the characteristics and limitations of the device were examined. In order to systematically characterize the fundamental performance of the spectrometer, a test ion was chosen. The choice was made based on four main criteria. It should be easy to produce and have a large mass in order to reduce the kinematic effect. The photodetachment process should also be confined to the lowest energy channel that leaves the residual atom in its ground state, and the photoelectron angular distribution should be characterized by an asymmetry parameter $\beta = 2$ independent of photon energy. For the first experiment using PEARLS, Cu^-, with a ground state configuration of $[Ar]3d^{10}4s^2$, was chosen. The electron affinity of the Cu atom is 1.236 eV corresponding to $\lambda \approx 1003$ nm [42]. A solid copper cathode was used to produce the negative ions. The choice to use the lighter isotope ^{63}Cu rather than ^{65}Cu was justified by the isotopic abundance ratio, approximately 70/30. A further investigation was later performed on $^{109}Ag^-$ with ground state configuration $[Kr]4d^{10}5s^2$. This ion also has $\beta = 2$ but almost twice the mass of $^{63}Cu^-$, and therefore a smaller kinematic effect. Ag has an electron affinity of 1.304 eV, giving a threshold at $\lambda \approx 951$ nm [42]. Kinematic

and angle acceptance corrections to the measurements were performed using the procedure described in 2.4.1.

4.1 Experimental setup

PEARLS was built for use at a synchrotron facility, but to be able to perform tests and modifications on the spectrometer it was necessary to install it elsewhere due to the limited beam time available at synchrotron beam lines. Since the project was a collaboration between ALS and the University of Gothenburg, the choice was made to install PEARLS at the Göteborg University Negative Ion Laser LAboratory GUNILLA, where ions and lasers are available. GUNILLA has been described in detail in other publications [43] but an overview will be given here. GUNILLA consists of a cesium sputter source and a system of ion optical components which makes it possible to create a narrow, mass-selected ion beam (Fig. 4.1). The laser enters the system antiparallel to the ion beam. The vacuum chamber containing PEARLS was mounted at the end of the ion beam path after a drift tube. An additional vacuum chamber with a quadrupole deflector, a Faraday cup (FC) for monitoring the ion current, and a neutral particle detector (NPD), was installed. The computer system of GUNILLA controls several parameters in the apparatus. These include the settings on the sputter ion source and electrical biases on the ion-optical elements, the CEM detectors, the NPD and the laser power meter. In addition, it was used to monitor the negative ion beam current as registered by the FC and the signals from the NPD, the CEMs and the laser power meter. In the measurements presented in Section 4.3.1, a 532 nm Nd:YAG laser with 20 Hz repetition rate was used. In the experiments described in Section 4.3.2, a Ti:Sa laser with 5 kHz repetition rate at $\lambda = 405$ nm was used.

4.1.1 Computer control and data acquisition

The first experiment using PEARLS was performed manually without the aid of a computer controlled data acquisition. This is of course a tedious task and requires a person on site for several hours if the repetition rate of the radiation source is relatively low. In the previous paragraph the computer controlled parts

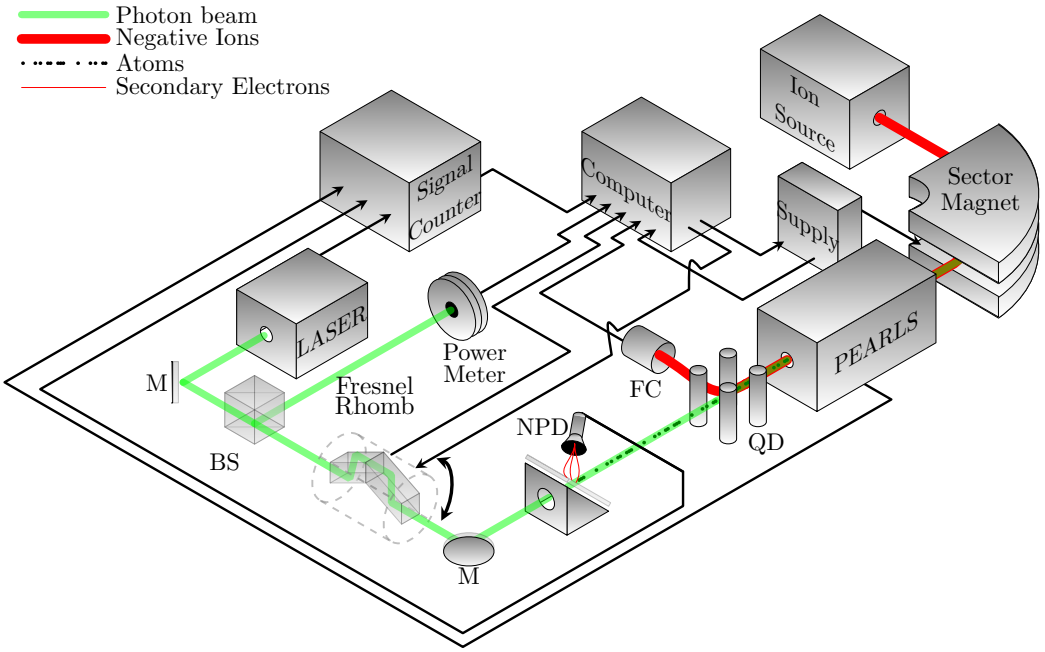

Figure 4.1: A schematic of the GUNILLA system as used in the experiments described in this thesis.

of GUNILLA were mentioned. PEARLS is, however, a separate system, and the eventual goal is to mount it on a synchrotron beamline. This would require a software control of its own. Therefore, prior to the second measurement, a data acquisition program was developed using LabVIEW. In order to obtain optimum settings for the signal counters, an investigation was made of the signal rate as a function of the time delay after the trigger pulse from the laser. This procedure helped to set the width of the time gates on the individual signal counters. Angular increments of the polarization rotation, acquisition time for each angle setting and other parameters are set prior to each measurement. The ion beam, with the laser blocked, was used as an isotropic source of photoelectrons, where collisional detachment randomly occur. The gain in pairs of opposite CEMs could then be set so that the average yield in both the vertical and the horizontal planes were equal, thereby compensating for differences in detection efficiency of the individual CEMs.

4.2 Simulations

To obtain corrections for the kinematic effect and acceptance angles of the spectrometer, the expected outputs of the CEMs 1-8 of the first and second detector planes of PEARLS were simulated with SIMION. A comparison with a simulation for the CEMs 5-8 of the second detector plane alone showed no differences. As a result, the detector plane using the four CEMs 5-8 were used in the test experiments. In order to perform the simulations in SIMION, an input array of photoelectron data was generated using MATLAB. First, approximately one million photoelectrons were randomly distributed in a cylindrical source. For a certain photon frequency ν, the same kinetic energy, $E_k = h\nu - E_A$, was assigned to all of the electrons. The velocity vectors were assumed to have a $\cos^2\theta$-distribution in the IF. The kinematic effect was then taken into account and the LF velocity vectors and kinetic energies of the photoelectrons were calculated. To simulate rotation of the polarization vector, the array generation procedure was repeated 18 times. For each additional array, an incremental angle, $\Delta\psi = n \cdot 10^\circ, n = 1 \ldots 18$, was added to the elevation of the velocity vectors. The expected output of the CEMs was then simulated in SIMION, and a value of the asymmetry parameter, $\widetilde{\beta}_{sim}$, was thus obtained. Fig. 4.2 shows the cumulative counts in all eight simulated CEMs as a function of ψ for a photon energy of $E_\gamma = 3.06$ eV. The simulation procedure described above was repeated for a number of different photon energies.

When the photoelectron energy tends to zero, the correction increases rapidly (Fig. 3.7). At $\lambda > 930$ nm, that is, a photoelectron energy $E_k = 0.029$ eV, no electrons were detected in the simulation.

4.3 Experimental results

The experiments presented here, in the next chapter and in Paper I, were performed using CEMs 5-8. In this section and in Paper I, CEMs 5-8 are sometimes labeled CEM_0, CEM_{90}, CEM_{180} and CEM_{270}, according to Fig. 3.1.

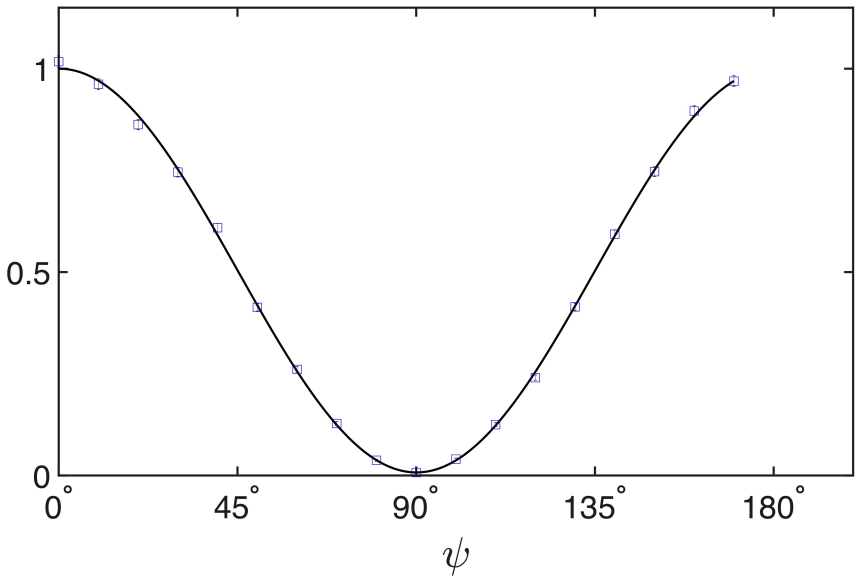

Figure 4.2: Simulation of the normalized LF yield of photolectrons from Ag^-, emitted in the IF with a $\cos^2\theta$-distribution. The curve through the simulated data points is a fit using Eq. 2.4. This yields a value of $\widetilde{\beta}_{sim} = 1.955 \pm 0.054$. This value corresponds to what would be expected in an experiment if PEARLS functioned according to the design.

4.3.1 Photodetachment from copper

The first successful measurement of the asymmetry parameter using PEARLS is displayed in Fig. 4.3. The data points were acquired by recording the CEM outputs of the signal counter while manually rotating the polarization vector of the photon beam using a Fresnel rhomb. Simulations of the experiment resulted in a value of $\widetilde{\beta}_{sim} = 1.931 \pm 0.05$. Together with the measurement, this indicated that the spectrometer performed as intended in spite of the rather primitive data collection procedure. The simulation and the experimental value $\widetilde{\beta}_{exp} = 1.801 \pm 0.13$ agree within the error bars, concluding that $\beta = 2$.

4.3.2 Photodetachment from silver

Fig. 4.4 shows the experimental results of photodetachment from Ag^- at $\lambda = 405$ nm. All data points were recorded using a custom made computer acquisition

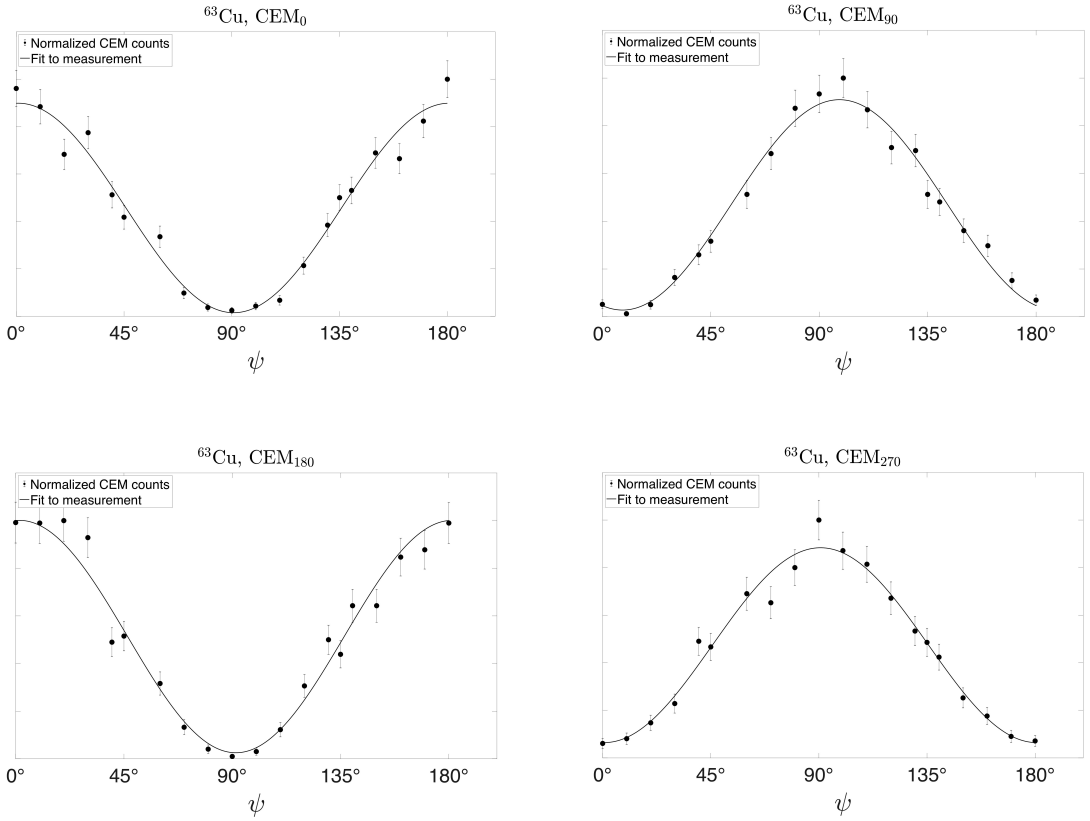

Figure 4.3: Results of the first PEARLS measurement that used four CEMs in one detector plane. The photodetachment of Cu^- is measured in four directions simultaneously. The solid curve through the data points is a fit to Eq. 2.4. It yields an experimental value of $\widetilde{\beta}_{exp} = 1.801 \pm 0.13$.

software. The measurements are fitted to Eq. 2.4 giving $\widetilde{\beta}_{exp} = 1.861 \pm 0.12$. A simulation of the experiment resulted in a value of $\widetilde{\beta}_{sim} = 1.955 \pm 0.054$, which agrees with $\widetilde{\beta}_{exp}$ within the error bars. As in the previous section, the conclusion that $\beta = 2$ for this system, can be drawn.

4.4 Discussion

The value obtained in a simulation that corrects for a kinematic effect and the geometric properties of the spectrometer, leading to a spread in IF emission angles, agrees with the measured value. This shows that PEARLS is capable

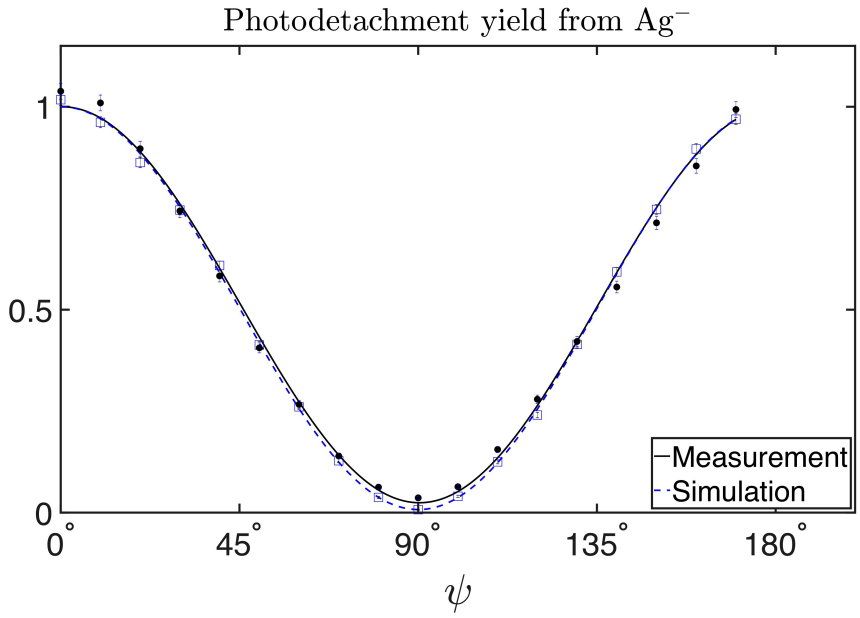

Figure 4.4: Normalized photoelectron intensity in CEM 5-8 added together, corresponding to $\widetilde{\beta}_{exp} = 1.861 \pm 0.12$. The simulated distribution with $\widetilde{\beta}_{sim} = 1.955 \pm 0.054$ from Fig. 4.2 is included for comparison.

of yielding reliable results. It works particularly well at higher photoelectron energies. A more detailed description of the Ag^- experiment can be found in Paper I.

5

Angular distribution of P^-

As shown in the previous chapter, photoelectron angular distributions can be measured using PEARLS. Of course, measuring a value which is already well known is only of interest when investigating the functionality of the spectrometer. The next step was to investigate a more complex problem, photodetachment of a bound p-state electron which involves a quantum mechanical interference between the resulting s- and d-waves in the final continuum state. This problem is of theoretical interest since it allows one to derive quantities such as the phase shift between the interfering waves. Specifically, the asymmetry parameter, β, which characterized the angular distribution pattern of the photoelectrons emitted in the photodetachment from P^- was investigated over a range of different photon energies. The P^- ground state configuration is [Ne]$3s^2 3p^4$. The ejection of the bound electron results in the production of s- and d-waves that interfere differently at different photon energies. About 20 years ago the angular distribution of P^- was measured at five wavelengths in the range 450-650 nm [44]. The electron affinity of P is 0.747 eV which corresponds to a wavelength of approximately 1660 nm. Significantly, the earlier measurement was unable to probe the low energy region, where a minimum occurs (Fig. 2.4) due to destructive interference between the s- and d-waves. As a result, the authors were unable to provide reliable values for the phase shift, c, and the size parameter, A_2 (see Eq. 2.6). A literature search indicated that in the previous measurement on P^-, the authors presented a larger value of the phase shift than had been reported

for analogous ions of the adjacent elements in the periodic table. The aim of the present experiment on P^- was to extend the energy range of the previous experiment to lower photon energies and, in particular, cover the region of the minimum and the approach to the threshold. By doing so, a fit to Eq. 2.6 would determine more reliable values for the c and A_2 parameters. As mentioned in Section 3.3.2, the low energy corrections to the kinematic effect will be large, putting the correction procedure to the test. The experimental setup for these measurements was the same as for the initial tests of the spectrometer, with the exception that additional lasers were used. In particular, an OPO of 10 Hz repetition rate was utilized in order to access the low photon energy region.
Fig. 5.1 shows the present measurements of the asymmetry parameter β as function of the kinetic energy of the photoelectrons in photodetachment from P^-.

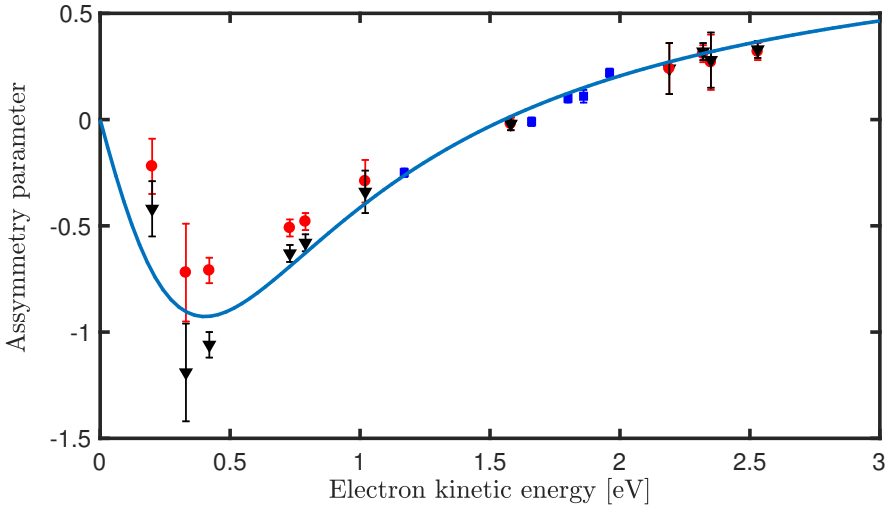

Figure 5.1: Angular distribution in the photodetachment from P^-. The blue squares denote the earlier data of Covington *et al.* [44]. The black triangles represent the raw data from the present experiment and the red circles show the raw data after it has been corrected for the kinematic effect and the non-zero acceptance angles of the PEARLS apparatus. The curve is a fit using Eq. 2.6.

The new data from the present measurement leads to some important conclusions. First, the phase shift between the outgoing s- and d-waves is close to zero, a result

which falls more in line with the published values from other elements in group IV through VII. It is therefore reasonable to assume that neither the atomic species nor the electron configuration affects the phase shift. Second, the parameter A_2 is shown to be a good measure of the spatial extension of the wave function of the ion. It varies between negative ions of different atomic species, but the electron affinity is also varying, and we have been able to show that these variations are correlated.

The large uncertainties at lower energies are mainly due to the low repetition rate of the laser, as well as the difficulty optimizing the spatial overlap of the ion and photon beams when infrared wavelengths are used. The large correction for the kinematic effect is clearly visible in the low energy data points. A more detailed description of the experiment can be found in Paper II.

6

Photoionization of Zn^+

So far in this work, we have only considered photodetachment of negative ions, and in particular, detachment of the extra electron. The photon energies necessary to perform such measurements are available through relatively low-cost sources such as tunable lasers, since the electron affinity of negative ions are at most a few eV. Of course, to fully understand the structure and dynamics of atoms, ions and molecules, this is not sufficient. The photon energies needed to investigate inner-shell photoionization are too high to be generated by laser sources. Synchrotron radiation sources, however, can produce photons in a continuous interval from far infrared up to x-rays. There are several synchrotron facilities around the globe. One of them is the Advanced Light Source (ALS) at Lawrence Berkeley National Laboratory in Berkeley, California, where the measurements described here and in Paper III were performed. The ALS synchrotron consists of an electron storage ring with 200 m circumference. A number of bending magnets force the electron beam to change its direction and thereby emit electromagnetic radiation tangentially to the orbit. After each bend, the energy lost through this process is regained by subjecting the electron beam to coaxial electric fields with an oscillation period synchronized with the passage of individual electron bunches. At ALS, there are over 40 beamlines with scientific endstations using the photon beams to examine various properties of matter. I was given the opportunity to participate in a photoionization experiment at the Ion-Photon Beamline (IPB) 10.0.1, the synchrotron endstation for which PEARLS

was originally built. A detailed description of the ALS IPB 10.0.1 can be found elsewhere [45].

There are several possible outcomes when a bound electron absorbs a high energy photon and escapes, leaving the residual system in an ionized state (or neutral, in the case of negative ions). If an inner-shell electron is removed, the hole in the electron configuration will be quickly filled by an electron from an outer shell. Fig. 6.1 shows two possible outcomes of such an event. For instance, energy can be released in the form of a photon, accompanied by the emission of so called Auger electrons. Spectroscopic investigations of the photons, as well as primary and secondary electrons reveal valuable information about the structure and dynamics of a positive ion.

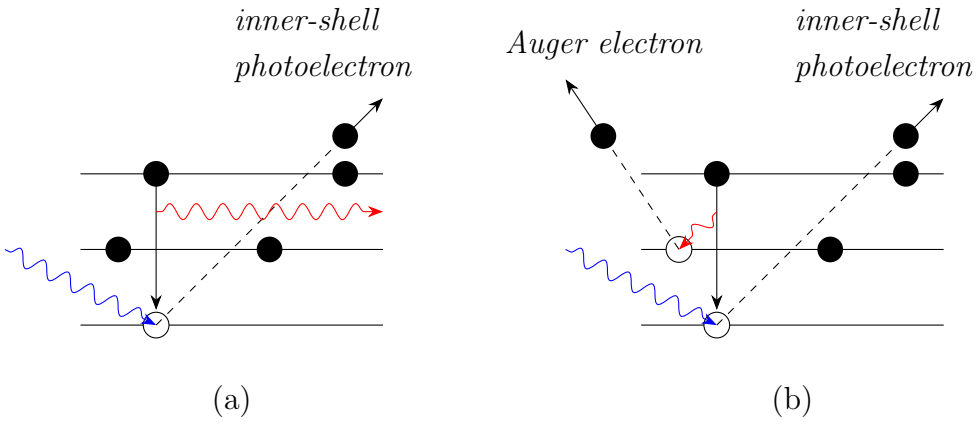

Figure 6.1: Schematic of two of the possible events that could arise when a high energy photon (blue) is absorbed by an inner-shell electron of an atom. (a) The emission of the inner-shell photoelectron which is replaced by an outer-shell electron through the emission of a photon (red). (b) Auger process, where the energy from the outer-shell electron is absorbed by another electron which then is ejected (Auger electron). Newly created holes in the inner structure of the ion could, of course, be filled by another electron, and new photons or Auger electrons may be emitted.

One of the main motivations for the photoionization experiment described in Paper III was to obtain benchmark data and theoretical models for a trans-Fe ion

which have shown to be of great interest in the studies of the chemical evolution of the Universe. In the experiment a merged beams technique was used, where a photon beam from an undulator in the synchrotron ring was overlapped in an Interaction Region (IR) by a 6 keV beam of Zn^+ ions from a cyclotron resonance source. The zinc was ionized through evaporation in an oven and later mixed with a buffer gas. After a series of electrostatic ion optical elements, the beam entered the IR which was voltage-biased in order to give the Zn^{2+} ions produced by photoionization a different kinetic energy than those produced elsewhere along the beam. By doing so, the photoionized ions were energy labelled. Using an analyzing magnet, the Zn^{2+} produced in the IR could then be separated from the original beam and counted. The intensities of the photon and ion beams were continuously recorded in order to correct for fluctuations in the photoionization signal. In addition to the experimental data, theoretical computations were performed for comparison. The absolute cross section measurements of the single photoionization of Zn^+ and the theoretical computations are in excellent agreement. Several different ionization channels could thereby be identified and characterized, as well as compared to previous experimental investigations. Considering the successful results of the total photoionization cross section of Zn^+, a natural next step would be to investigate the differential cross sections of the ionization channels, a task for which PEARLS would be well suited.

7

Conclusions and outlook

The aim of this work was to design and perform tests on an angle-resolved photoelectron spectrometer, and later also utilize the system to investigate photoelectron angular distributions. The initial tests and the measurements performed shows that the spectrometer is a powerful tool when it comes to examining wide range energy dependence of the asymmetry parameter, β, that characterizes the shape of the photoelectron emission pattern following photodetachment. The collinear geometry is an essential feature of the device. This yields a large photoelectron production rate, making the spectrometer especially suitable for experimental investigations where the beam time is a limiting factor. One of the main motivations to initiate the PEARLS project was to build a photoelectron spectrometer which would provide a high signal to noise ratio at a synchrotron facility, where the signal is normally low. From the results of this work, it is clear that PEARLS meets these expectations and can become a useful part of any synchrotron beamline endstation at which it will be placed. The spectrometer is also equipped with a high pass filter which has been shown to have the ability to suppress low energy photoelectrons arising from channels involving excited states of the residual atom. Close to the threshold, a large kinematic effect is present and this affects the experimental results. A workable solution to correct for this experimental error has been developed using computer simulations, and it has proven to also work at higher energies. The spectrometer is designed to have electrostatic analyzers in front of the CEMs. When these are manufactured and

mounted, PEARLS can be used to measure asymmetry parameters for specific photodetachment channels.
So far, the spectrometer has been tested on negative ions of a few different atomic species using lasers that generate different wavelengths, with data acquisition from four CEMs simultaneously. The next step would be to mount all 16 CEMs and incorporate the energy analyzer. The system would then be ready for installation at a synchrotron facility, such as ASTRID2 in Århus, Denmark [46], or MAX IV in Lund, Sweden [47]. Another option is to combine it with a Movable Ion-Photon Beamline (MIPB) [48] in order to perform experiments at different sites.

Acknowledgements

First, I would like to thank Kammarkollegiet, the Swedish Research Council and MAX4ESSFUN for financial support of my employment as a PhD student, and the U.S. Department of Energy for the financing of PEARLS. Without their contributions, this work would not have come to be. I would also like to thank my employer, Donnergymnasiet, for letting me spend so much time in the lab instead of teaching. I would also like to thank Alex Aguilar, former beamline scientist at beamline 10.0.1, who initiated the project and took good care of me when I first visited LBNL.

There will not be a thesis and a licentiate degree without a supervisor. Dag Hanstorp has been an invaluable support, source of knowledge and experience, and a good friend. From our collaboration, is clear that frequent coffee breaks is one of the key ingredients in making good science.

Writing about science requires a lot of work, and it is not trivial to summarize several years of experimental investigations into less than 60 pages. I have had great help from Prof. D.J. Pegg, University of Tennessee, who spent many hours going through my texts both for the individual papers and this thesis. Thank you so much for your input, and enjoy the beach!

A special thanks to Johan Rohlén, with whom I shared office the first period of my time at Chalmers/GU. Without your help, I would never have been able to perform a single measurement. Your knowledge around the lab was invaluable for a rookie, and you seemed to have infinite time and patience available.

His office seat was replaced by Jakob Welander, who has been a great colleague and a friend during many hours at floor 8. Your sweet tooth has not been good for me, though, but I guess we can fix that if we ever make it out for a long distance run.

The licentiate studies was part of a project led by Karin Ekman and Per Lundgren, to whom I owe a thank you for organizing events and several opportunities to meet other teachers in research oriented discussions.

There are many more people around the lab who I could thank, but the list would be very long if I named all of them. However, I should mention Jan-Åke Wiman and Mats Rostedt for the technical support, and Oscar Isaksson for coffee drinking support and great collaboration on the hand-in exercises of the MATLAB course.

Last, but definitely not least, I thank Anna-Karin, for putting up with all this. Without your support, I would never have come this far.

References

[1] E. Becquerel. Mémoire sur les effets électriques produits sous l'influence des rayons solaires. *Comptes Rendus*, 9:561–567, 1839.

[2] H. Hertz. Ueber einen Einfluss des ultravioletten Lichtes auf die electrische Entladung. *Annalen der Physik und Chemie*, 267(8):983–1000, 1887.

[3] P. Lenard. Ueber die lichtelektrische Wirkung. *Annalen der Physik*, 1902.

[4] A. Einstein. On a Heuristic Point of View about the Creation and Conversion of Light. *Annalen der Physik*, 17(132):91, 1905.

[5] F. Reinert and S. Hufner. Photoemission spectroscopy - from early days to recent applications. *New Journal of Physics*, 7:34, 2005.

[6] D. J. Pegg. Structure and dynamics of negative ions. *Reports on Progress in Physics*, 67(6):857–905, 2004.

[7] K. Siegbahn and K. Edvarson. β-Ray Spectroscopy in the Precision Range of 1:10^5. *Nuclear Physic*, 1(8):137–159, 1 1956.

[8] S. Hagström, C. Nordling, and K. Siegbahn. Electron spectroscopy for chemical analyses. *Physics Letters*, 9(3):235–236, 4 1964.

[9] C. S. Fadley. X-ray photoelectron spectroscopy: Progress and perspectives. *Journal of Electron Spectroscopy and Related Phenomena*, 178-179(C):2–32, 2010.

[10] A. Kothe, J. Metje, M. Wilke, A. Moguilevski, N. Engel, R. Al-Obaidi, C. Richter, R. Golnak, I. Y. Kiyan, and E. F. Aziz. Time-of-flight electron spectrometer for a broad range of kinetic energies. *Review of Scientific Instruments*, 84(2):1–7, 2013.

[11] P. Kruit and F. H. Read. Magnetic field paralleliser for 2π electron-spectrometer and electron-image magnifier. *Journal of Physics E: Scientific Instruments*, 1983.

[12] D. M. Neumark. Slow Electron Velocity-Map Imaging of Negative Ions: Applications to Spectroscopy and Dynamics. *Journal of Physical Chemistry A*, 112(51):13287–13301, 2008.

[13] A. Osterwalder, M. J. Nee, J. Zhou, and D. M. Neumark. High resolution photodetachment spectroscopy of negative ions via slow photoelectron imaging. *Journal of Chemical Physics*, 121(13):6317–6322, 2004.

[14] C. Blondel, C. Delsart, and F. Dulieu. The photodetachment microscope. *Physical Review Letters*, 77(18):3755–3758, 1996.

[15] D. Strickland and G. Mourou. Compression of amplified chirped optical pulses. *Optics Communications*, 1985.

[16] I. Y. Kiyan, U. Berzinsh, J. Sandstrom, D. Hanstorp, and D. J. Pegg. Spectrum of doubly excited states in the K^- ion. *Physical Review Letters*, 84(26):5979–5982, 2000.

[17] M. Eklund, H. Hultgren, D. Hanstorp, and I. Y. Kiyan. Orbital alignment in atoms generated by photodetachment in a strong laser field. *Physical Review A - Atomic, Molecular, and Optical Physics*, 88(2), 2013.

[18] L. M. Branscomb, D. S. Burch, S. J. Smith, and S. Geltman. Photodetachment cross section and the electron affinity of atomic oxygen. *Physical Review*, 111(2):504–513, 1958.

[19] K. Michishio, T. Tachibana, H. Terabe, A. Igarashi, K. Wada, T. Kuga, A. Yagishita, T. Hyodo, and Y. Nagashima. Photodetachment of positronium negative ions. *Physical Review Letters*, 106(15), 2011.

[20] S. J. Cavanagh, S. T. Gibson, and B. R. Lewis. Photodetachment of O^- from threshold to 1.2 eV electron kinetic energy using Velocity-Map Imaging. In *International Symposium on (e,2e), Double Photoionization and Related Topics / 15th International Symposium on Polarization and Correlation in Electronic and Atomic Collisions*, volume 212 of *Journal of Physics Conference Series*, 2010.

[21] P. O'Keeffe, P. Bolognesi, A. Mihelic, R. Richter, A. Moise, E. Ovcharenko, G. C. King, and L. Avaldi. Application of a VMI spectrometer to near-threshold photoionization with synchrotron radiation. *Journal of Physics: Conference Series*, 288(1):012020, 2011.

[22] M. Hand, H. Wang, S. S. Dhesi, K. Sawhney, and IUCr. Investigation of the polarization state of dual APPLE-II undulators. *Journal of Synchrotron Radiation*, 23(1):176–181, 1 2016.

[23] S. AlMoussalami, J. M. Bizau, B. Rouvellou, D. Cubaynes, L. Journel, F. J. Wuilleumier, J. Obert, J. C. Putaux, T. J. Morgan, and M. Richter. First angle-resolved photoelectron measurements following inner-shell resonant excitation in a singly charged ion. *Physical Review Letters*, 76(24):4496–4499, 1996.

[24] D. Hanstorp, M. Gustafsson, U. Berzinsh, and U. Ljungblad. Collinear photodetachment spectroscopy. *Nuclear Instruments & Methods in Physics Research Section B-Beam Interactions with Materials and Atoms*, 79(1-4):159–161, 1993.

[25] O. Windelius, A. Aguilar, R. C. Bilodeau, A. M. Juarez, I. Rebolledo-Salgado, D. J. Pegg, J. Rohlén, T. Castel, J. Welander, and D. Hanstorp. A collinear angle-resolved photoelectron spectrometer. *Nuclear Instruments and Methods in Physics Research, Section B: Beam Interactions with Materials and Atoms*, 410:144–152, 2017.

[26] U. Boesl and W. J. Knott. Negative ions, mass selection, and photoelectrons. *Mass Spectrometry Reviews*, 17(4):275–305, 1998.

[27] M. Yavor. Electrostatic Energy Analyzers. *Advances in Imaging and Electron Physics*, 157:213–258, 2009.

[28] A. Eppink and D. H. Parker. Velocity map imaging of ions and electrons using electrostatic lenses: Application in photoelectron and photofragment ion imaging of molecular oxygen. *Review of Scientific Instruments*, 68(9):3477–3484, 1997.

[29] J. M. Bizau, D. Cubaynes, M. Richter, F. J. Wuilleumier, J. Obert, J. C. Putaux, T. J. Morgan, E. Kallne, S. Sorensen, and A. Damany. 1st observation of photoelectron spectra emitted in the photoionization of a singly charged ion beam with synchrotron radiation. *Physical Review Letters*, 67(5):576–579, 1991.

[30] R. C. Bilodeau and H. K. Haugen. Experimental studies of Os^-: Observation of a bound-bound electric dipole transition in an atomic negative ion. *Physical Review Letters*, 85(3):534–537, 2000.

[31] C. W. Walter, N. D. Gibson, Y. G. Li, D. J. Matyas, R. M. Alton, S. E. Lou, Field III R. L., D. Hanstorp, L. Pan, and D. R. Beck. Experimental and theoretical study of bound and quasibound states of Ce. *Physical Review A*, 84(3), 2011.

[32] P. Andersson, A. O. Lindahl, C. Alfredsson, L. Rogstrom, C. Diehl, D. J. Pegg, and D. Hanstorp. The electron affinity of phosphorus. *Journal of Physics B-Atomic Molecular and Optical Physics*, 40(20):4097–4107, 2007.

[33] E. P. Wigner. On the behavior of cross sections near thresholds. *Physical Review*, 73(9):1002–1009, 1948.

[34] T. J. Millar, C. Walsh, and T. A. Field. Negative ions in space. *Chemical Reviews*, 117(3):1765–1795, 2017.

[35] J. Cooper and R. N. Zare. Angular Distribution of Photoelectrons. *The Journal of Chemical Physics*, 48(2):942–943, 1 1968.

[36] H A Bethe. Handbuch der Physik, vol. 24/1. *Julius Springer, Berlin*, 1933.

[37] D Hanstorp, C Bengtsson, and D J Larson. Angular distributions in photodetachment from O-. *Physical Review A*, 40(2):670–675, 1989.

[38] M. Bydder, A. Rahal, G. D. Fullerton, and G. M. Bydder. The magic angle effect: A source of artifact, determinant of image contrast, and technique for imaging. *Journal of Magnetic Resonance Imaging*, 25(2):290–300, 2007.

[39] M. W. Siegel, R. A. Bennett, R. J. Celotta, J. L. Hall, and J. Levine. Molecular photodetachment spectrometry 1. Electron affinity of nitric-oxide and molecular constants of NO. *Physical Review A*, 6(2):607–631, 1972.

[40] Scientific Instrument Services Inc. (www.simion.com). SIMION v8.1.

[41] D. Hanstorp. An ion beam apparatus for collinear photodetachment experiments. *Nuclear Instruments & Methods in Physics Research Section B-Beam Interactions with Materials and Atoms*, 100(1):165–175, 1995.

[42] R. C. Bilodeau, M. Scheer, and H. K. Haugen. Infrared laser photodetachment of transition metal negative ions: studies on Cr^-, Mo^-, Cu^- and Ag^-. *Journal of Physics B: Atomic, Molecular and Optical Physics*, 31(17):3885–3891, sep 1998.

[43] C. Diehl, K. Wendt, A. O. Lindahl, P. Andersson, and D. Hanstorp. Ion optical design of a collinear laser-negative ion beam apparatus. *Review of Scientific Instruments*, 82(5):7, 2011.

[44] A. M. Covington, D. Calabrese, W. W. Williams, J. S. Thompson, and T. J. Kvale. Measurements of photoelectron angular distributions by single-photon detachment of Al^-, Si^-, and P^- at visible photon wavelengths. *Physical Review A*, 56(6):4746–4754, 1997.

[45] A. Aguilar, A. M. Covington, G. Hinojosa, R. A. Phaneuf, I. Alvarez, C. Cisneros, J. D. Bozek, I. Dominguez, M. M. Sant'Anna, A. S. Schlachter, S. N. Nahar, and B. M. McLaughlin. Absolute Photoionization Cross Section Measurements of O II Ions from 29.7 to 46.2 eV. *The Astrophysical Journal Supplement Series*, 146(2):467–477, 2003.

[46] S. P. Møller, J. S. Nielsen, and N. Hertel. ASTRID2 - The New Low-emittance Light Source in Denmark. *Proceedings of the 1st International Particle Accelerator Conference, IPAC2012, Kyoto*, p:2487–2489, 2010.

[47] P. F. Tavares, E. Al-Dmour, Å. Andersson, F. Cullinan, B. N. Jensen, D. Olsson, D. K. Olsson, M. Sjöström, H. Tarawneh, S. Thorin, and A. Vorozhtsov. Commissioning and first-year operational results of the MAX IV 3GeV ring. *Journal of Synchrotron Radiation*, 25(5):1291–1316, 2018.

[48] N. D. Gibson, C. W. Walter, R. L. Field, D. J. Carman, J. Z. Shapiro, R. C. Bilodeau, I. Dumitriu, N. Berrah, and A. Aguilar. Inner-shell photodetachment from Se^- negative ions at the ALS. *Journal of Physics: Conference Series*, 2009.